



HAL
open science

An extended finite element solution for hydraulic fracturing with thermo-hydro-elastic–plastic coupling

Qingdong Zeng, Jun Yao, Jianfu Shao

► **To cite this version:**

Qingdong Zeng, Jun Yao, Jianfu Shao. An extended finite element solution for hydraulic fracturing with thermo-hydro-elastic–plastic coupling. *Computer Methods in Applied Mechanics and Engineering*, 2020, 364, pp.112967 -. 10.1016/j.cma.2020.112967 . hal-03489609

HAL Id: hal-03489609

<https://hal.science/hal-03489609>

Submitted on 8 Mar 2022

HAL is a multi-disciplinary open access archive for the deposit and dissemination of scientific research documents, whether they are published or not. The documents may come from teaching and research institutions in France or abroad, or from public or private research centers.

L'archive ouverte pluridisciplinaire **HAL**, est destinée au dépôt et à la diffusion de documents scientifiques de niveau recherche, publiés ou non, émanant des établissements d'enseignement et de recherche français ou étrangers, des laboratoires publics ou privés.



Distributed under a Creative Commons Attribution - NonCommercial 4.0 International License

An extended finite element solution for hydraulic fracturing with thermo-hydro-elastic-plastic coupling

Qingdong Zeng^{a,b,c}, Jun Yao^b, Jianfu Shao^{c,*}

^a*Department of Mechanics, College of Energy and Mining Engineering, Shandong University of Science and Technology, Qingdao, China*

^b*Research Center of Multiphase Flow in Porous Media, China University of Petroleum (East China), Qingdao, China*

^c*LaMcube, UMR9013, CNRS, University of Lille, Lille, France*

Abstract

In this study, we present an efficient numerical solution for studying hydraulic fracturing under coupled thermal-hydraulic conditions in an elastic-plastic porous medium. The propagation of macroscopic fracture is described by using an extended finite element method. Both the fluid flow through the porous medium and the exchange between the medium and fracture are taken into account. It is the same for the heat transfer. An efficient iterative scheme is then proposed to deal with the coupling between material deformation with fracture growth, fluid flow and heat transfer. The proposed method is assessed through comparisons with analytical solutions for a number of well-established problems. A series of numerical calculations are further performed in order to investigate the effect of plastic deformation and temperature change on the process of hydraulic fracture propagation.

Keywords: Hydraulic fracturing; Cold fluid injection; THM coupling; Plastic deformation; Extended finite element method

Nomenclature

*Corresponding author: jian-fu.shao@polytech-lille.fr

$\boldsymbol{\sigma}$	total stress tensor
$\boldsymbol{\sigma}'$	Biot's effective stress tensor
\mathbf{b}	body force vector
$\boldsymbol{\varepsilon}$	total strain tensor
$d\boldsymbol{\varepsilon}$	total strain increment
$d\boldsymbol{\varepsilon}^e, d\boldsymbol{\varepsilon}^p, d\boldsymbol{\varepsilon}^\theta$	elastic, plastic and thermal strain increment
$d\boldsymbol{\sigma}$	stress increment
\mathbf{C}	elastic stiffness matrix
α	Biot's coefficient
p	pore fluid pressure
\mathbf{I}	second-order identity tensor
K_D	bulk modulus
T	temperature
$\mathbf{s}(\boldsymbol{\sigma}')$	deviatoric stress
J_2	second invariant of deviatoric stress
I_1	first invariant of principal stress
η, ζ	rock plastic parameters
ϕ	internal friction angle
c	cohesion
H_v, H_t	rock hardening parameters
$d\gamma$	plastic multiplier
$\mathbf{C}^{ep}, \mathbf{C}^h$	consistent elasto-plastic tensors
m, f	subscripts denoting the matrix and fracture, respectively
M	Biot's modulus
q_{mf}	fluid cross-flow between matrix and fracture
S_m	area of matrix element
\mathbf{v}_m	fluid velocity in the matrix
k_m	matrix permeability

μ	fluid dynamic viscosity
α_m	thermal fluid mass change coefficient
α_f	linear thermal expansion coefficient of fluid
α_s	linear thermal expansion coefficient of solid
ϕ_m	porosity of matrix
ξ	point position in the fracture
w_f	fracture width
S_f	area of fracture element
Q_0	fluid injection rate
L_f	fracture length
k_{mf}	effective permeability between matrix element and fracture segment
A_{mf}	contact area of matrix element and fracture segment
l_{mf}	contact length of matrix element and fracture segment
\bar{d}	mean vertical distance of nodes in the matrix element with respect to the fracture
d_n	vertical distance of one point in the matrix element with respect to the fracture
ρ	equivalent density of porous matrix
c_m	equivalent heat capacity of porous matrix
λ	equivalent thermal conductivity of porous matrix
ε_v	volume strain
h_{mf}	heat exchange between matrix and fracture
s, f	subscripts denoting the solid and fluid, respectively
v_f	fluid velocity in the fracture
h_t	heat transfer coefficient
\mathbf{t}_d	cohesive traction
\mathbf{T}	tangential stiffness matrix of traction-separation law
\mathbf{u}^h	approximated displacement function
\mathbf{x}	point position vector
\mathbf{I}^n	set of all nodes

I^{cr}	set of nodes whose support element is cut off by the crack
N_i	shape function
Δu_i	standard degree increment
Δa_i	enriched degree increment
$H(\cdot)$	Heaviside step function
$\varphi(\cdot)$	signed distance function
σ_0	reference stress
ε_0	reference strain
a_r, n_r	material constants
r, θ	polar coordinate frame of fracture tip
$\delta(\Delta \mathbf{u})$	virtual displacement increment
$[[\delta(\Delta \mathbf{u})]]$	virtual displacement jump between fracture surfaces
σ_v	mean total stress
E	elastic modulus
ν	Poisson's ratio

5 1. Introduction

Hydraulic fracturing is a key technical solution for the enhancement of oil and gas production through enlarging drainage volume, especially for tight reservoirs with very low permeability (Li et al., 2014; Fan et al., 2019). It also plays a critical role in many other applications, such as CO₂ geological sequestration (Papanastasiou et al., 2016a; Fu et al., 2017), nuclear waste disposal (de Laguna, 1966), exploitation of enhanced geothermal system (AbuAisha et al., 2016) and exploitation of coal-bed methane. Great efforts have been dedicated to studying its mechanism, simulating the propagation kinetics and retrieving fracture parameters (Bohlooli and Pater, 2006; Lecampion, 2009; Zhang et al., 2007; Zhu et al., 2015; Zhang et al., 2018; Wang et al., 2019). Generally, the initial temperature of reservoir is higher than that of the injected fluid. It is reported that the thermal cooling effect reduces fracture pressure and fracture length but increases fracture width (Feng et al., 2016). Further, new fractures or secondary fracture may be induced by cooling process,

known as thermal-induced fractures (Arogundade et al., 2016). The cryogenic fracturing with liquid nitrogen has been experimentally and numerically studied to investigate the mechanism of ultra-low temperature induced fracture process (Yao et al., 2017a, 2017b). This implies that the thermal effect on hydraulic fracturing needs to be considered. On the other hand, many rocks in under-compacted reservoirs exhibit elastic-plastic deformation and their mechanical behavior is affected by pore pressure and temperature change (Han et al., 2018). The hydraulic fracturing process is governed by a thermo-hydro-elastic-plastic (THEP) coupling problem. Therefore, it is necessary to develop a THEP coupling model for hydraulic fracturing in order to better understand the physical mechanisms involved and to cover various scenarios.

Traditionally, hydraulic fracturing models are split into three ingredients: fluid flow in fracture, rock deformation analysis and crack propagation. The key issue and main difference between various models lie on the description of rock deformation analysis. Due to the discontinuity related to fracture, the rock deformation is handled by different kinds of numerical methods. For instance, the displacement discontinuity method (DDM) describes the relationship between fracture width and the stress acting on its surface based on an analytical solution derived by Crouch et al. (1983). The application of DDM to hydraulic fracturing can be found in Weng et al. (2011), Wu et al. (2015), Zeng and Yao (2016) and references therein. The extended finite element method (XFEM) is very convenient for modeling the displacement jump across a fracture by introducing additional enrichment functions to the standard shape functions. The pioneering work of adopting XFEM to fluid flow modeling in fractured deformable porous media was made by Réthoré et al. (2007a, 2007b, 2008). They have proposed a two-scale model to couple the fluid flow in the cavity of fracture at the micro-scale with that flow in the porous medium at the macro-scale, and then modeled the propagation of cohesive crack and shear bands. Other recent studies using XFEM for hydraulic fracture modeling can be seen in Mohammadnejad and Khoei (2013), Dahi-Taleghani and Olson (2011) and Zeng et al. (2018). Either in the DDM or in the XFEM, a fracture is explicitly represented as a strong discontinuity, which can be categorized as a discontinuous approach. A discontinuous approach requires additional

criteria to determine when a crack grows in which direction, and the discontinuity surface has to be explicitly tracked, which becomes an intractable task for those problems with complex crack paths. Alternative solutions have been provided by continuous approaches. As two
50 typical ones, phase field method (Aranson et al., 2000; Zhu et al., 2019; Zhou et al., 2019a; Brun et al., 2020) and peridynamic method (Silling, 2000) have received a considerable attention during recent years. We do not intend to give a detailed discussion on those methods and relevant studies about their application to hydraulic fracturing can be found in Mikelic et al. (2015), Heider and Markert (2016), Wilson and Landis (2016), Zhou et al.
55 (2019b), Chukwudozie et al. (2019) and references therein. However, both the phase field and peridynamics methods do not explicitly consider displacement discontinuities across fractures.

The seepage of fluid from fracture into rock matrix increases pore pressure around fracture, leading to an expansion of rock matrix. This will result in the so-called back-stress
60 onto fracture. Moreover, cooling of rock formation during hydraulic fracturing with cold fluid may decrease total stress in reservoir, which results in the reduction of fracture pressure. Therefore, the hydraulic fracture propagation depends on the interplay between pore pressure, temperature and stress. In the recent decades, more and more studies have been conducted to investigate the poroelastic effect or thermoelastic effect on hydraulic fracturing.
65 For instance, (Réthoré et al., 2008) presented a two-scale model for cohesive crack propagation in a deformable porous medium as mentioned above. Other studies can be found in Mohammadnejad and Khoei (2013), McClure et al. (2016), Salimzadeh et al. (2017) and Zeng et al. (2019b), which provided different methods for modeling of fluid flow in fracture and matrix. In particular, in Zeng et al. (2019b) a hybrid approach coupling the extended
70 finite element method and embedded discrete fracture model (XFEM-EDFM) has been presented to model fracture propagation in poroelastic medium. This hybrid XFEM-EDFM approach was initially introduced for coupled geomechanics and multiphase flow in naturally fractured porous media (Ren et al., 2016, 2018), where fractures were not allowed to propagate. The advantage of this method is that both displacement and fluid pressure can
75 be solved using the same embedded mesh. In addition, AbuAisha et al. (2016) simulated

hydraulic fracturing process within a thermo-poroelastic framework for enhanced geothermal system. Feng et al. (2016) embedded a thermal module in the simulator FLAC3D to account for the thermal effect on hydraulic fracturing. All these models assume a linear elastic constitutive relation between stress and strain. However, significant plastic deformation can occur in a number of reservoirs rocks such as sandstone and shales. Even though a few studies have been devoted to accounting for the effect of plastic deformation (Papanastasiou et al., 1997, 1999, 2016b; Sarris and Papanastasiou, 2013; Wang, 2015; Zeng et al., 2019a), the full thermo-hydro-elasto-plastic coupling effect on hydraulic fracturing has rarely so far investigated.

In terms of numerical strategy, there are two aspects closely related to thermo-hydro-mechanical (THM) coupling problems: the numerical solution for each physical field and the overall solution strategy for all coupled fields. The finite volume method and finite difference method are widely used in modeling fluid flow and heat transfer, and the finite element method is a popular method in the analysis of mechanical deformation. These methods have been extended and improved for some complex THM coupling problems. For example, the mimetic finite difference method and multi-scale finite element method have been presented to simulate fluid flow in an anisotropic medium and in a strongly heterogeneous medium respectively (Huang et al., 2014; Yalchin and Thomas, 2008). When the reservoir is abundant with fractures, fluid flow in small scale fractures is represented by multi-continuum methods (such as multiple interacting continua method, dual porosity and dual permeability models). Meanwhile, fluid flow in large scale fractures is captured by discrete fracture models or embedded discrete fracture models (EDFM) (Yan et al., 2016, 2019). As to the solution strategy for all fields, there are several approaches, such as fully implicit, explicit coupling and iterative coupling Settari et al. (2001). Among these approaches, the fixed stress split iterative scheme has been proved to be unconditionally stable and quite suitable for THM coupling problems (Kim et al., 2011; Garipov et al., 2018).

The main novelty of this study is to develop an efficient numerical method to investigate fracture propagation in saturated porous media by considering the full coupling between

105 temperature change, fluid flow and elastic-plastic deformation by using the hybrid XFEM-EDFM approach. Both of fluid flow and heat transfer in fractured media are considered and solved by an embedded discrete fracture model. Elastic-plastic deformation of porous rock is analyzed by using the extended finite element method without remeshing during the process of hydraulic fracture propagation. The fixed stress split scheme is adopted to solve
 110 mechanical-hydraulic-thermal fields and an efficient overall iterative solution algorithm is proposed. The proposed numerical model is validated against analytical solutions for several well-established benchmark cases. The effects of plastic deformation and heat transfer on hydraulic fracturing are analyzed through a number of numerical studies.

2. Problem statement and governing equations

115 We consider here the propagation of a discrete fracture in a saturated porous medium exhibiting an elastic-plastic behavior and subjected to mechanical loading, fluid flow and temperature change. We shall determine the deformation and stress fields, pressure and temperature fields and the evolution with time of fracture length.

2.1. Mechanical problem

120 We adopt here the assumption of small strains and quasi static loading for solving the mechanical problem. The static equilibrium equations are written as:

$$\nabla \cdot \boldsymbol{\sigma} + \mathbf{b} = \mathbf{0} \quad (1)$$

where $\boldsymbol{\sigma}$ is the total stress tensor and \mathbf{b} is the body force vector.

Due to the plastic deformation and temperature change, the total incremental strain $d\boldsymbol{\varepsilon}$ is decomposed into three parts: the elastic incremental strain $d\boldsymbol{\varepsilon}^e$, the plastic incremental
 125 strain $d\boldsymbol{\varepsilon}^p$ and the thermal incremental strain $d\boldsymbol{\varepsilon}^\theta$:

$$d\boldsymbol{\varepsilon} = d\boldsymbol{\varepsilon}^e + d\boldsymbol{\varepsilon}^p + d\boldsymbol{\varepsilon}^\theta \quad (2)$$

The total incremental stress in the saturated porous medium is related to the elastic incremental strain and incremental pore fluid pressure, that is:

$$d\boldsymbol{\sigma} = \mathbf{C} : d\boldsymbol{\varepsilon}^e - \alpha dp \mathbf{I} \quad (3)$$

where \mathbf{C} is the drained elastic stiffness matrix. α denotes the Biot's coefficient, and p is the pore fluid pressure. \mathbf{I} is the second-order identity tensor. According to the strain repartition
130 given in Equation (2), the elastic incremental strain is given by:

$$d\boldsymbol{\varepsilon}^e = d\boldsymbol{\varepsilon} - d\boldsymbol{\varepsilon}^p - d\boldsymbol{\varepsilon}^\theta \quad (4)$$

Substituting Equation (4) into Equation (3), the following thermo-poro-elastic-plastic relation is obtained:

$$d\boldsymbol{\sigma} = \mathbf{C} : (d\boldsymbol{\varepsilon} - d\boldsymbol{\varepsilon}^p) - \alpha dp \mathbf{I} - \mathbf{C} : d\boldsymbol{\varepsilon}^\theta \quad (5)$$

Furthermore, the thermal incremental strain can be related to the temperature change increment. The constitutive relation (5) becomes:

$$d\boldsymbol{\sigma} = \mathbf{C} : (d\boldsymbol{\varepsilon} - d\boldsymbol{\varepsilon}^p) - \alpha dp \mathbf{I} - 3\alpha_s K_D dT \mathbf{I} \quad (6)$$

135 where K_D is the drained bulk modulus. α_s is the linear thermal expansion coefficient of porous medium, and T is the temperature. In this study, we shall put the emphasis on the influence of plastic deformation and thermal deformation and fluid pressure change due to temperature variation. Therefore, for the sake of clarity, we will neglect the variation of elastic properties with temperature and the elastic stiffness matrix \mathbf{C} remains constant in
140 the whole loading history. However, the dependance of elastic properties on temperature variation can be easily taken into account in the proposed numerical model with an explicit scheme.

For the description of plastic deformation, a plastic model with a Drucker-Prager type criterion is here adopted. In order to account for the effect of pore fluid pressure on plastic
145 deformation, the plastic yield criterion is here formulated in terms of Biot's effective stress $\boldsymbol{\sigma}' = \boldsymbol{\sigma} + \alpha p \mathbf{I}$, and it is expressed as follows:

$$f(\boldsymbol{\sigma}') = \sqrt{J_2(\mathbf{s}(\boldsymbol{\sigma}'))} + \eta I_1(\boldsymbol{\sigma}') - \zeta \leq 0 \quad (7)$$

where $\mathbf{s}(\boldsymbol{\sigma}')$ denotes the deviatoric stress tensor, and J_2 is its second invariant. I_1 is the first invariant of the effective stress tensor. The two strength parameters η and ζ can be related

to the internal friction angle and cohesion defined in the classical Mohr-Coulomb criterion:

$$\eta = \frac{2 \sin \phi}{\sqrt{3} (3 \pm \sin \phi)} \quad (8)$$

$$\zeta = \frac{6c \cos \phi}{\sqrt{3} (3 \pm \sin \phi)} \quad (9)$$

where ϕ and c denote the internal friction angle and the cohesion, respectively. The plus and minus signs respectively correspond to the inner and outer approximation of the Mohr-Coulomb hexagon yield surface by the Drucker-Prager circular yield surface.

It is further assumed that the porous material exhibits both plastic hardening and thermal hardening. This is interpreted by the variation of cohesion as a function of plastic volumetric strain and temperature, defined as follows:

$$dc = H_v d\varepsilon_v^p - H_t dT \quad (10)$$

where H_v and H_t are two hardening parameters. ε_v^p is the plastic volumetric strain.

On the other hand, putting the emphasis of our study on the description of fracture propagation under coupled thermo-hydro-plastic conditions, an associated plastic flow rule is here assumed. Therefore, the plastic strain increment is given by the following flow rule:

$$d\varepsilon^p = d\gamma \frac{\partial f}{\partial \boldsymbol{\sigma}'} \quad (11)$$

where $d\gamma$ is the plastic multiplier, and $\frac{\partial f}{\partial \boldsymbol{\sigma}'}$ indicates the plastic flow vector. From Equation (6), the effective stress increment can be expressed by

$$d\boldsymbol{\sigma}' = \mathbf{C} : (d\varepsilon - d\varepsilon^p) - 3\alpha_s K_D dT \mathbf{I} \quad (12)$$

The yield function (7) must further satisfy the following consistency condition:

$$\frac{\partial f}{\partial \boldsymbol{\sigma}'} : d\boldsymbol{\sigma}' + \frac{\partial f}{\partial \zeta} d\zeta = 0 \quad (13)$$

According to the hardening law, the evolution of function $d\zeta$ can be related to that of plastic volumetric strain and temperature. Substituting Equations (11) and (12) into Equation (13) yields

$$\frac{\partial f}{\partial \boldsymbol{\sigma}'} : \left(\mathbf{C} : d\varepsilon - \mathbf{C} : d\gamma \frac{\partial f}{\partial \boldsymbol{\sigma}'} - 3\alpha_s K_D dT \mathbf{I} \right) + \frac{\partial f}{\partial \zeta} \left(\frac{\partial \zeta}{\partial \varepsilon_v^p} d\varepsilon_v^p + \frac{\partial \zeta}{\partial T} dT \right) = 0 \quad (14)$$

As the plastic volumetric strain increment is given by $d\varepsilon_v^p = 3\eta d\gamma$, the plastic multiplier $d\gamma$ is expressed as follows:

$$d\gamma = \frac{\frac{\partial f}{\partial \sigma'} : \mathbf{C} : d\varepsilon - \frac{\partial f}{\partial \sigma'} : 3\alpha_s K_D dT \mathbf{I} + \frac{\partial f}{\partial \zeta} \frac{\partial \zeta}{\partial T} dT}{\frac{\partial f}{\partial \sigma'} : \mathbf{C} : \frac{\partial f}{\partial \sigma'} - 3\eta \frac{\partial f}{\partial \zeta} \frac{\partial \zeta}{\partial \varepsilon_v^p}} \quad (15)$$

The substitution of Equations (11) and (15) for Equation (12) gives the following incremental effective stress, strain and temperature relation:

$$d\sigma' = \mathbf{C}^{ep} : d\varepsilon - \mathbf{C}^h dT \quad (16)$$

$$\mathbf{C}^{ep} = \mathbf{C} - \frac{\left(\mathbf{C} : \frac{\partial f}{\partial \sigma'}\right) \otimes \left(\frac{\partial f}{\partial \sigma'} : \mathbf{C}\right)}{\frac{\partial f}{\partial \sigma'} : \mathbf{C} : \frac{\partial f}{\partial \sigma'} - 3\eta \frac{\partial f}{\partial \zeta} \frac{\partial \zeta}{\partial \varepsilon_v^p}} \quad (17)$$

$$\mathbf{C}^h = \frac{\left(\mathbf{C} : \frac{\partial f}{\partial \sigma'}\right) \left(\frac{\partial f}{\partial \sigma'} : 3\alpha_s K_D \mathbf{I} - \frac{\partial f}{\partial \zeta} \frac{\partial \zeta}{\partial T}\right)}{\frac{\partial f}{\partial \sigma'} : \mathbf{C} : \frac{\partial f}{\partial \sigma'} - 3\eta \frac{\partial f}{\partial \zeta} \frac{\partial \zeta}{\partial \varepsilon_v^p}} + 3\alpha_s K_D \mathbf{I} \quad (18)$$

where \mathbf{C}^{ep} is the fourth order tangent elastic-plastic operator in the isothermal condition while \mathbf{C}^h is the second order coupling tensor between effective stress and temperature change.

According to Equations (9) and (10), the derivatives of ζ with respect to plastic volumetric strain and temperature change are given by

$$\frac{\partial \zeta}{\partial \varepsilon_v^p} = \frac{6 \cos \phi}{\sqrt{3} (3 \pm \sin \phi)} \frac{\partial c}{\partial \varepsilon_v^p} = \frac{6 \cos \phi}{\sqrt{3} (3 \pm \sin \phi)} H_v \quad (19)$$

$$\frac{\partial \zeta}{\partial T} = \frac{6 \cos \phi}{\sqrt{3} (3 \pm \sin \phi)} \frac{\partial c}{\partial T} = \frac{6 \cos \phi}{\sqrt{3} (3 \pm \sin \phi)} H_T \quad (20)$$

The incorporation of these relations into Equations (17) and (18) leads to the final expressions of tangent elastic-plastic operator and coupling tensor:

$$\mathbf{C}^{ep} = \mathbf{C} - \frac{\left(\mathbf{C} : \frac{\partial f}{\partial \sigma'}\right) \left(\frac{\partial f}{\partial \sigma'} : \mathbf{C}\right)}{\frac{\partial f}{\partial \sigma'} : \mathbf{C} : \frac{\partial f}{\partial \sigma'} - 3\eta \frac{\partial f}{\partial \zeta} \frac{6 \cos \phi}{\sqrt{3} (3 \pm \sin \phi)} H_v} \quad (21)$$

$$\mathbf{C}^h = \frac{\left(\mathbf{C} : \frac{\partial f}{\partial \sigma'}\right) \left(\frac{\partial f}{\partial \sigma'} : 3\alpha_s K_D \mathbf{I} - \frac{\partial f}{\partial \zeta} \frac{6 \cos \phi}{\sqrt{3} (3 \pm \sin \phi)} H_T\right)}{\frac{\partial f}{\partial \sigma'} : \mathbf{C} : \frac{\partial f}{\partial \sigma'} - 3\eta \frac{\partial f}{\partial \zeta} \frac{6 \cos \phi}{\sqrt{3} (3 \pm \sin \phi)} H_v} + 3\alpha_s K_D \mathbf{I} \quad (22)$$

2.2. Fluid flow

The fluid flow in the fractured system is composed of the flow through the porous matrix and inside the fracture. The fracture is embedded into the porous matrix through a nonconforming grid. The cross flow between the fracture and porous matrix is also taken
 185 into account.

2.2.1. Flow through porous matrix

Considering the effect of volumetric strain and thermal expansion, the equation of conservation is expressed as

$$\frac{1}{M} \frac{\partial p_m}{\partial t} + \alpha \nabla \cdot \frac{\partial \mathbf{u}}{\partial t} + \nabla \cdot \mathbf{v}_m = \frac{q_{mf} \delta_{mf}}{S_m} + 3\alpha_m \frac{\partial T_m}{\partial t} \quad (23)$$

where p_m is the pore fluid pressure in the matrix. M is the Biot's modulus. q_{mf} denotes
 190 the cross flow between matrix and fracture, which is given in the following section. δ_{mf} is the Delta function, which equals to 1 only when the fracture crosses the matrix element. S_m is the area of matrix element. T_m is the temperature in the matrix. The first two terms account for the change in the porous skeleton, the third term represents the outflow from control volume, and the fourth term is cross flow from fracture segment. The last terms
 195 represents the thermal expansion due to temperature variation.

In Equation (23), \mathbf{v}_m is the velocity of fluid in the matrix, which is here described by Darcy's conduction law.

$$\mathbf{v}_m = -\frac{k_m}{\mu} \cdot \nabla p_m \quad (24)$$

where k_m is the permeability of matrix, and μ is the dynamic viscosity of fluid.

In Equation (23), α_m denotes the thermal fluid mass change coefficient. It is the sum of
 200 the thermal expansion of the fluid and that of the solid matrix. By assuming that the thermal expansion of the solid matrix is equal to that of the bulk material in drained condition, one gets the following approximation of α_m :

$$\alpha_m = (\alpha - \phi_m) \alpha_s + \phi_m \alpha_f \quad (25)$$

where α_f, α_s are, respectively, the coefficients of linear thermal expansion of fluid and solid. ϕ_m is the porosity of the solid matrix.

In this study, the embedded discrete fracture model (EDFM) (Yan et al., 2016, 2019) is used to simulate fluid flow and heat transfer (presented in the next section) in fractured porous media. Similar to XFEM model for solving mechanical problems, the advantage of the EDFM model is that the domain is meshed independent of the fracture location. Therefore, we here try to combine the common advantage these two methods by using XFEM to solve the stress field and EDFM to the pressure and temperature fields. However, there is a significant difference between two methods. In the frame of XFEM, additional DOFs are introduced to the grid nodes and no discretization is needed for the fracture (2007a, 2007b). In the EDFM, the domain is meshed firstly as independent of the fracture, and then the fracture is discretized into finite segments. No additional DOFs are introduced to the grid nodes but introduced to fracture segment points instead. The efficiency of the proposed combined EDFM-XFEM methods will be verified through comparisons with some analytical solutions. In the frame of EDFM model, the fluid velocity q through the cross section of fracture is written as

$$q = -\frac{w_f^3}{12\mu} \frac{\partial p_f}{\partial \xi} \quad (26)$$

where ξ is the distance along the fracture. p_f is the fluid pressure in the fracture. w_f is the fracture width.

The distribution of fluid pressure in fracture is controlled by three main factors including the fracture width variation, fluid compressibility and thermal expansion. However, during the process of fracture propagation, the effect of fracture volume variation is predominate over the effects of other two factors. Therefore, the conservation equation adopted here only considers the variation of fracture width:

$$\frac{\partial q}{\partial \xi} + \frac{\partial w_f}{\partial t} + \frac{q_{mf}}{l_{mf}} = 0 \quad (27)$$

where l_{mf} denotes the contact length of the matrix element and fracture segment. The first term represents the outflow from control volume in a given fracture segment. The second term accounts for incremental fluid due to the fracture width variation. The last term represents the fluid leakoff from fracture to matrix.

The boundary condition for the fluid flow in fracture is such that the injection rate is prescribed at the inlet point of the fracture, which can be written as

$$q_f(0) = Q_0 \quad (28)$$

where Q_0 is the given fluid injection rate. Based on the local mass conservation equation, the global conservation equation can be formulated as follows:

$$\int_0^t Q_0 dt = \int_0^{L_f} w ds + \int_0^t q_{mf} dt \quad (29)$$

where L_f is the whole length of the fracture.

It is essential to determine the expression of cross flow between matrix and fracture elements for the purpose of connecting fluid pressure between the matrix and fracture. According to the embedded discrete fracture model, the cross flow between matrix and fracture can be given under the assumption of steady flow as shown in Fig. 1.

$$q_{mf} = \frac{2k_{mf}A_{mf}}{\mu} \nabla p = \frac{2k_{mf}l_{mf}}{\mu} \frac{p_f - p_m}{\bar{d}} \quad (30)$$

where p_f , p_m are the fluid pressure in fracture segment and matrix element respectively. k_{mf} is the effective permeability between matrix element and fracture segment, which can be approximated by the harmonic average of permeability of matrix element and fracture segment. A_{mf} is the contact area of the matrix element and the fracture segment. In this study, a two-dimension model is considered, the fracture is a line segment, and the contact area A_{mf} is replaced by the contact length between matrix element and fracture segment l_{mf} .

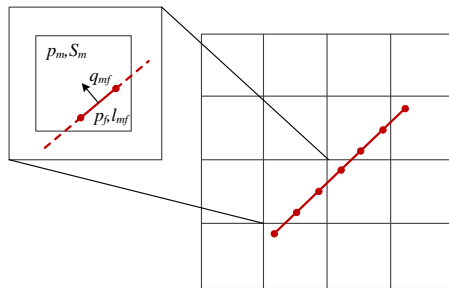


Figure 1: Illustration of cross flow between matrix element and fracture segment

In Equation (30), \bar{d} is the average normal distance of nodes in the matrix element with respect to the fracture, which is expressed by

$$\bar{d} = \frac{\int_{S_m} d_n dS}{S_m} \quad (31)$$

where d_n is the normal distance of one point in the matrix element with respect to the fracture.

2.3. Heat transfer

Similar to fluid flow, the heat transfer in the fractured system is also composed of the heat transfer through the matrix, in the fracture and the cross heat exchange between the two components.

2.3.1. Heat transfer through matrix

It is assumed that the variation of temperature in the matrix is directly caused by the heat exchange between matrix and fracture, and there is no other heat source in the matrix. As the fluid velocity in the matrix is much smaller than that in the fracture, it is thus assumed that the heat transfer in the matrix is dominated by thermal conduction. Therefore, the classical equation to describe heat transfer in the rock mass only considering heat conduction is given as follows:

$$\rho c_m \frac{\partial T_m}{\partial t} + 3\alpha_s K_d T_0 \frac{\partial \varepsilon_v}{\partial t} - 3\alpha_m T_0 \frac{\partial p_m}{\partial t} - \lambda \nabla^2 T_m = \frac{h_{mf} \delta_{mf}}{S_m} \quad (32)$$

where T_m is the temperature in matrix. ρ , c_m and λ are the equivalent values of mass density, heat capacity and thermal conductivity of the saturated porous matrix respectively. ε_v is the mechanical volumetric strain. h_{mf} is the heat exchange term between matrix and fracture. S_m is the area of matrix element, the same as the one in Equation (23).

The equivalent thermal parameters can be expressed as the weighted average of the properties of the solid matrix and the fluid as follows

$$\rho c_m = (1 - \phi_m) \rho_s c_s + \phi_m \rho_f c_f \quad (33)$$

$$\lambda = (1 - \phi_m) \lambda_s + \phi_m \lambda_f \quad (34)$$

where the subscripts s , f denote the solid matrix and fluid.

270 *2.3.2. Heat transfer in fracture*

Similar to the fluid flow in fracture, the heat transfer only takes place along the direction of fracture propagation. As the fluid velocity in the fracture can be large enough, heat convection should be taken into consideration. The equation of heat transfer in the fracture can be written as:

$$\rho_f c_f \frac{\partial T_f}{\partial t} + \rho_f c_f v_f \frac{\partial T_f}{\partial \xi} - \lambda_f \frac{\partial^2 T_f}{\partial \xi^2} + \frac{h_{mf}}{S_f} = 0 \quad (35)$$

275 where ξ and S_f are the distance and area of fracture segment, the same as those in Equation (27). The fluid velocity v_f in Equation (35) is determined by the fluid flow in fracture with the following expression:

$$v_f = -\frac{w_f^2}{12\mu} \frac{\partial p_f}{\partial \xi} \quad (36)$$

On the other hand, the heat exchange between matrix and fracture is depicted by using a form of Newton's law of cooling, which is expressed as

$$h_{mf} = h_t A_{mf} (T_f - T_m) \quad (37)$$

280 where h_t is the heat transfer coefficient, and A_{mf} is the contact area between the matrix element and the fracture segment, replaced by the contact length l_{mf} in two dimension cases, the same as the one in Equation (30).

2.4. Fracture propagation criterion

In this study, the plastic strain is considered, which gives rise to fracture process zone
285 ahead of the crack tip. Besides, the thermal strain is also taken into account. To account for these strains, the cohesive crack model is used to determine crack propagation here. The cohesive crack concept has been widely used for crack nucleation and propagation in quasi-brittle and ductile materials. The numerical simulation of cohesive crack propagation within the XFEM frame has been carried out in the literature.

290 In the cohesive crack model, the fracture process zone is characterized by a traction-separation law that describes the relationship between cohesive traction and displacement jump, which can be written as

$$\mathbf{t}_d = \mathbf{t}_d([\mathbf{u}]) \quad (38)$$

where \mathbf{t}_d is the cohesive traction across the cohesive surface, $\llbracket \mathbf{u} \rrbracket$ the corresponding displacement jump across the discontinuity.

295 To be consistent with the incremental finite element formulation in the following section, the differential form of cohesive relation is used as follows.

$$d\mathbf{t}_d = \mathbf{T} d\llbracket \mathbf{t} \rrbracket \quad (39)$$

where \mathbf{T} is the tangential stiffness matrix of the traction-separation law.

The linear softening law is employed in this study. There are two critical parameters for the cohesive crack model, one is the cohesive strength σ_c and the other one is the cohesive
300 fracture energy G_c . The cohesive fracture energy equals to the area under the traction-separation curve. When the energy release rate attains the cohesive fracture energy, crack extension occurs. In this study, the hydraulic fracture is assumed to propagate in static or quasi static regime, as widely considered in the literature. The switch between tensile and shear fracture in dynamic crack propagation regime is ignored. Furthermore, for the
305 sake of simplicity, the effect of plastic strain on crack propagation direction, studied in some previous studies (Remmers et al., 2008), is also neglected. Therefore, it is assumed that the crack always propagates perpendicularly to the maximum hoop stress direction, as widely adopted in elastic cases (Erdogan and Sih, 1963). On the other hand, due to the discontinuity of crack and inspired by some previous studies (Elguedj et al., 2006, 2007),
310 the sub-quadrangle partitioning technique (Ji et al., 2002) and the geometrical subdividing method (Elguedj et al., 2007) are here combined and used for the numerical integration of elastic-plastic crack propagation problem. The radius of the geometrical subdividing is also chosen in the way as presented in the study (Elguedj et al., 2007) based on the radius of the plastic zone and fracture toughness. We divide the nearby element surrounding the crack
315 into 25 sub-quadrangle and use 25 Gaussian points as shown in Figure 2. This method avoids projection of stress and internal variables for different loading steps. In addition, the phantom nodes method is used for crack propagation evaluation. This method has been used for simulation of arbitrary crack propagation, and proven to exhibit almost no mesh dependency if the mesh is sufficiently refined (Rabczuk et al., 2008; Remmers et al., 2008;

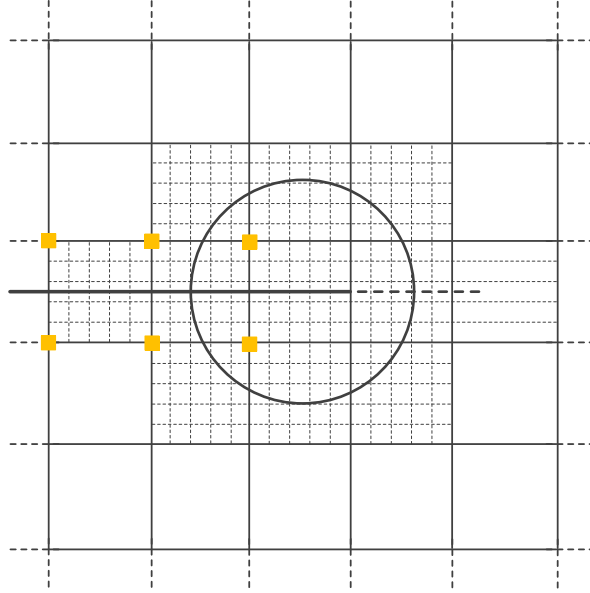


Figure 2: Geometrical sub-dividing of elements around the fracture

3. Numerical method and solution strategy

3.1. Displacement field by extended finite element method

Due to the displacement jump through fracture surfaces, the extended finite element method is here adopted to determine displacement field. To be consistent with the cohesive zone model, the tip enrichment is ignored and only the discontinuous enrichment is considered in the approximation (Wang, 2015). An incremental formulation of displacement approximation is given as follows:

$$\Delta \mathbf{u}^h(\mathbf{x}) = \sum_{i \in \mathbf{I}^n} N_i(\mathbf{x}) \Delta u_i + \sum_{i \in \mathbf{I}^{\text{cr}}} N_i(\mathbf{x}) (H(\varphi(\mathbf{x})) - H(\varphi(\mathbf{x}_i))) \Delta a_i \quad (40)$$

where \mathbf{x} is the point position vector. \mathbf{I}^n is the set of all nodes. \mathbf{I}^{cr} is the set of nodes whose support element is cut off by a crack. N_i is the shape function. Δu_i is the standard nodal displacement increment. Δa_i denotes the enriched nodal displacement jump increment. $\varphi(\cdot)$ is the signed distance function, and $H(\cdot)$ is the Heaviside function.

Due to the nonlinear stress-strain relation, the prescribed load history is split into a number of small increments. For the loading increment from i_k to i_{k+1} , the integral weak form can be obtained by the virtual work principle as follows:

$$\int_{\Omega} \delta(\nabla_s(\Delta \mathbf{u})) : (\Delta \boldsymbol{\sigma}' + \boldsymbol{\sigma}^{i_k}) d\Omega - \alpha \int_{\Omega} \delta(\nabla_s(\Delta \mathbf{u})) : (\Delta p_m + p_m^{i_k}) \mathbf{I} d\Omega = \int_{\Omega} \delta(\Delta \mathbf{u}) \cdot (\Delta \mathbf{b} + \mathbf{b}^{i_k}) d\Omega$$

$$+ \int_{\Gamma_t} \delta(\Delta \mathbf{u}) \cdot (\Delta \bar{\mathbf{t}} + \bar{\mathbf{t}}^{i_k}) d\Gamma + \int_{\Gamma_f} \llbracket \delta(\Delta \mathbf{u}) \rrbracket \cdot [(\Delta \mathbf{t}_d + \mathbf{t}_d^{i_k}) - (\Delta p_f + p_f^{i_k}) \mathbf{n}_{\Gamma_f}] d\Gamma \quad (41)$$

where $\delta(\Delta \mathbf{u})$ is the virtual displacement increment. $\llbracket \delta(\Delta \mathbf{u}) \rrbracket$ is the displacement jump between fracture surfaces, which is given by

$$\llbracket \delta(\Delta \mathbf{u}) \rrbracket = \delta(\Delta \mathbf{u})^+ - \delta(\Delta \mathbf{u})^- \quad (42)$$

The stress increment $\Delta \boldsymbol{\sigma}'$ in Equation (41) is expressed by the displacement increment and temperature increment as shown in Equation (16):

$$\Delta \boldsymbol{\sigma}' = \mathbf{C}^{ep} : \nabla_s(\Delta \mathbf{u}) - \mathbf{C}^h \Delta T \quad (43)$$

The tangent operators \mathbf{C}^{ep} and \mathbf{C}^h vary during the given loading history, leading to the nonlinearity of the set of discrete equations given above. Thus, the well-known Newton-Raphson method is adopted to determine the displacement increment for each increment step. Further, the implicit elastic predictor/plastic corrector return-mapping algorithm is chosen for numerical integration of general elastic-plastic constitutive relations. The method has shown great convergence and stability. The details of return mapping algorithm with consideration of thermal effect are illustrated in Appendix A.

3.2. THM coupling process

In order to facilitate the solution of thermo-hydro-mechanical coupling process, we shall adopt here the fixed mean stress scheme. The mean total stress σ_v remains unchanged between the thermo-hydro-mechanical coupling iteration from l to $l + 1$, that is:

$$\sigma_v^{l+1} - \sigma_v^l = 0 \quad (44)$$

On the other hand, the mean total stress can be expressed in terms of volumetric strain, fluid pressure and temperature changes as follows:

$$\sigma_v^{l+1} - \sigma_v^l = K_d (\varepsilon_v^{l+1} - \varepsilon_v^l) - \alpha (p^{l+1} - p^l) - 3\alpha_s K_d (T^{l+1} - T^l) \quad (45)$$

where ε_v is the volumetric strain. From Equations (44) and (45), the volumetric strain variation during the coupling iteration can be written by

$$\varepsilon_v^{l+1} - \varepsilon_v^l = \frac{\alpha}{K_d} (p^{l+1} - p^l) + 3\alpha_s (T^{l+1} - T^l) \quad (46)$$

3.2.1. Fluid pressure field

According to the fluid flow equation in the matrix (Eq. 23), the temporal discretization can be written as follows

$$\frac{1}{M} \frac{\partial p_m^{n+1,l+1}}{\partial t} + b \frac{\partial \varepsilon_v^{n+1,l+1}}{\partial t} - 3\alpha_m \frac{\partial T_m^{n+1,l+1}}{\partial t} - \frac{k_m}{\mu} \nabla^2 p_m^{n+1,l+1} = \frac{q_{mf}^{n+1,l+1} \delta_{mf}}{S_m} \quad (47)$$

where n is the time step number, and l is the iteration step number during the time step from n to $n+1$.

Substituting Equations (30) and (46) into Equation (47) gives the temporal discretization of fluid pressure field based on the fixed mean stress scheme as follows:

$$\begin{aligned} \left(\frac{1}{M} + \frac{\alpha^2}{K_d} \right) \frac{\partial p_m^{n+1,l+1}}{\partial t} - \frac{k_m}{\mu} \nabla^2 p_m^{n+1,l+1} + (3\alpha_s - 3\alpha_m) \frac{\partial T_m^{n+1,l+1}}{\partial t} + \frac{\delta_{mf} T_{mf} p_m^{n+1,l+1}}{S_m} \\ - \frac{\delta_{mf} T_{mf} p_f^{n+1,l+1}}{S_m} = -\alpha \frac{\partial \varepsilon_v^{n+1,l}}{\partial t} + \frac{\alpha^2}{K_d} \frac{\partial p_m^{n+1,l}}{\partial t} + 3\alpha_s \frac{\partial T_m^{n+1,l}}{\partial t} \end{aligned} \quad (48)$$

With regard to the fluid flow in the fracture (Eq. 27), the temporal discretization can be expressed as follows

$$\frac{(w_f^{n+1,l})^3}{12\mu} \frac{\partial^2 p_f^{n+1,l+1}}{\partial \xi^2} - \frac{T_{mf} p_f^{n+1,l+1}}{l_{mf}} + \frac{T_{mf} p_m^{n+1,l+1}}{l_{mf}} = \frac{\partial w_f^{n+1,l}}{\partial t} \quad (49)$$

3.2.2. Temperature field

Similar to the fluid pressure field, the temporal discretization of temperature field can be derived. The discretized equation of heat transfer in the matrix (Eq. 32) is written as

$$\rho c \frac{\partial T_m^{n+1,l+1}}{\partial t} + 3\alpha_s K_d T_0 \frac{\partial \varepsilon_v^{n+1,l+1}}{\partial t} - 3\alpha_m T_0 \frac{\partial p_m^{n+1,l+1}}{\partial t} - \lambda \nabla^2 T_m^{n+1,l+1} = \frac{h_{mf}^{n+1,l+1} \delta_{mf}}{S_m} \quad (50)$$

Substituting Equations (37) and (46) into Equation (50) gives the temporal discretization of temperature field based on the fixed mean stress scheme as follows

$$\begin{aligned}
& (\rho c + 9\alpha_s^2 K_d T_0) \frac{\partial T_m^{n+1,l+1}}{\partial t} + (3\alpha_s T_0 - 3\alpha_m T_0) \frac{\partial p_m^{n+1,l+1}}{\partial t} - \lambda \nabla^2 T_m^{n+1,l+1} + \frac{\delta_{mf} h_t l_{mf}}{S_m} T_m^{n+1,l+1} \\
& - \frac{\delta_{mf} h_t l_{mf}}{S_m} T_f^{n+1,l+1} = -3\alpha_s K_d T_0 \frac{\partial \varepsilon_v^{n+1,l}}{\partial t} + 9\alpha_s^2 K_d T_0 \frac{\partial T_m^{n+1,l}}{\partial t} + 3\alpha_s T_0 \frac{\partial p^{n+1,l}}{\partial t} \quad (51)
\end{aligned}$$

As for the heat transfer in the fracture, the temporal discretization of Equation (35) is expressed as

$$\rho_f c_f \frac{\partial T_f^{n+1,l+1}}{\partial t} + \rho_f c_f v_f \frac{\partial T_f^{n+1,l+1}}{\partial \xi} - \lambda_f \frac{\partial^2 T_f^{n+1,l+1}}{\partial \xi^2} + \frac{h_c l_{mf} T_f^{n+1,l+1}}{S_f} - \frac{h_c l_{mf} T_m^{n+1,l+1}}{S_f} = 0 \quad (52)$$

The velocity term v_f in Equation (52) is related to the fluid pressure in the fracture, which indicates that the whole equations of pressure and temperature fields are nonlinear.

Therefore, an iterative scheme is needed to solve the coupling equations.

3.2.3. Iterative scheme for coupling solution

A simple iterative scheme is here proposed to solve the fluid pressure and temperature fields. To determine the pressure and temperature values at the iteration step $l + 1$, their values at the iteration step l are taken as the initial values ($k = 1$). The fluid pressure equation is solved by using the previous step temperature value, and then the temperature is updated with the newly obtained pressure value. The loop is repeated until the relative errors between two consecutive steps becomes less than a desired tolerance. The obtained values are taken as the results of iteration $l + 1$.

Accounting for this iteration scheme, we rewrite the temporally discretized equations of fluid flow in the matrix and fracture (Eqs. 47, 49) by omitting the superscript $(n + 1, l + 1)$ as follows

$$\begin{aligned}
& \left(\frac{1}{M} + \frac{\alpha^2}{K_d} \right) \frac{\partial p_m^{k+1}}{\partial t} - \frac{k_m}{\mu} \nabla^2 p_m^{k+1} + \frac{\delta_{mf} T_{mf} p_m^{k+1}}{S_m} - \frac{\delta_{mf} T_{mf} p_f^{k+1}}{S_m} = -\alpha \frac{\partial \varepsilon_v^{n+1,l}}{\partial t} + \frac{\alpha^2}{K_d} \frac{\partial p_m^{n+1,l}}{\partial t} \\
& + 3\alpha_s T_0 \frac{\partial T_m^{n+1,l}}{\partial t} - (3\alpha_s - 3\alpha_m) \frac{\partial T_m^k}{\partial t} \quad (53)
\end{aligned}$$

$$\frac{(w_f^{n+1,l})^3}{12\mu} \frac{\partial^2 p_f^{k+1}}{\partial \xi^2} - \frac{T_{mf} p_f^{k+1}}{l_{mf}} + \frac{T_{mf} p_m^{k+1}}{l_{mf}} = \frac{\partial w_f^{n+1,l}}{\partial t} \quad (54)$$

To derive the spatial discretization of Equations (53) and (54), the divergence term of pressure in the matrix and fracture is approximated as

$$\begin{aligned} \nabla^2 p_{m,ij} &= \frac{1}{\Delta x} \left(\frac{\partial p_{m,i+\frac{1}{2}j}}{\partial x} - \frac{\partial p_{m,i-\frac{1}{2}j}}{\partial x} \right) + \frac{1}{\Delta y} \left(\frac{\partial p_{m,ij+\frac{1}{2}}}{\partial y} - \frac{\partial p_{m,ij-\frac{1}{2}}}{\partial y} \right) \\ &= \frac{1}{\Delta x^2} (p_{m,i-1j} - 2p_{m,ij} + p_{m,i+1j}) + \frac{1}{\Delta y^2} (p_{m,ij-1} - 2p_{m,ij} + p_{m,ij+1}) \end{aligned} \quad (55)$$

$$\begin{aligned} \frac{\partial^2 p_{f,i}}{\partial \xi^2} &= \frac{1}{\Delta \xi_i} \left(\frac{\partial p_{f,i+1/2}}{\partial \xi} - \frac{\partial p_{f,i-1/2}}{\partial \xi} \right) = \frac{1}{2\Delta \xi_i (\Delta \xi_i + \Delta \xi_{i+1})} p_{f,i+1} \\ &+ \frac{1}{2\Delta \xi_i (\Delta \xi_i + \Delta \xi_{i-1})} p_{f,i-1} - \left(\frac{1}{2\Delta \xi_i (\Delta \xi_i + \Delta \xi_{i+1})} + \frac{1}{2\Delta \xi_i (\Delta \xi_i + \Delta \xi_{i-1})} \right) p_{f,i} \end{aligned} \quad (56)$$

The fluid pressures in the matrix and fracture are solved simultaneously, and the final discretized equations can be written in the matrix form as

$$\begin{bmatrix} \mathbf{H}_m + \mathbf{T}_m + \mathbf{R}_{mf} & -\mathbf{R}_{mf} \\ -\mathbf{R}_{fm} & \mathbf{T}_f + \mathbf{R}_{fm} \end{bmatrix} \begin{bmatrix} \mathbf{p}_m^{k+1} \\ \mathbf{p}_f^{k+1} \end{bmatrix} = \begin{bmatrix} \mathbf{F}_m \\ \mathbf{F}_f \end{bmatrix} \quad (57)$$

where \mathbf{p}_m^{k+1} and \mathbf{p}_f^{k+1} are the vectors of fluid pressure values in the matrix and fracture. \mathbf{T}_m and \mathbf{T}_f are the conductivity coefficient matrixes of fluid pressure in the matrix and fracture systems derived from Equations (55) and (56). The expressions of other sub-matrixes \mathbf{H}_m , \mathbf{R}_{mf} , \mathbf{R}_{fm} , \mathbf{F}_m and \mathbf{F}_f are listed in Appendix B.

Likewise, the temporal discretization of heat transfer equations in the matrix and fracture is expressed as

$$\begin{aligned} (\rho c + 9\alpha_s^2 K_d T_0) \frac{\partial T_m^{k+1}}{\partial t} - \lambda \nabla^2 T_m^{k+1} + \frac{\delta_{mf} h_t l_{mf}}{S_m} T_m^{k+1} - \frac{\delta_{mf} h_t l_{mf}}{S_m} T_f^{k+1} &= -3\alpha_s K_d T_0 \frac{\partial \varepsilon_v^{n+1,l}}{\partial t} \\ + 9\alpha_s^2 K_d T_0 \frac{\partial T_m^{n+1,l}}{\partial t} + 3\alpha_s T_0 \frac{\partial p^{n+1,l}}{\partial t} - (3\alpha_s T_0 - 3\alpha_m T_0) \frac{\partial p_m^{k+1}}{\partial t} \end{aligned} \quad (58)$$

$$\rho_f c_f \frac{\partial T_f^{k+1}}{\partial t} - \rho_f c_f \frac{w_f^2}{12\mu} \frac{\partial p_f^{k+1}}{\partial \xi} \frac{\partial T_f^{k+1}}{\partial \xi} - \lambda_f \frac{\partial^2 T_f^{k+1}}{\partial \xi^2} + \frac{h_t l_{mf} T_f^{k+1}}{S_f} - \frac{h_t l_{mf} T_m^{k+1}}{S_f} = 0 \quad (59)$$

To get the spatial discretization of temperature field in the matrix (Eq. 58), the divergence of temperature is approximated by

$$\nabla^2 T_{m,ij} = \frac{1}{\Delta x^2} (T_{m,i-1j} - 2T_{m,ij} + T_{m,i+1j}) + \frac{1}{\Delta y^2} (T_{m,ij-1} - 2T_{m,ij} + T_{m,ij+1}) \quad (60)$$

Similarly, the divergence of temperature in the fracture (Eq. 59) is discretized as

$$\begin{aligned} \frac{\partial^2 T_{f,i}}{\partial \xi^2} &= \frac{1}{2\Delta\xi_i (\Delta\xi_i + \Delta\xi_{i+1})} T_{f,i+1} + \frac{1}{2\Delta\xi_i (\Delta\xi_i + \Delta\xi_{i-1})} T_{f,i-1} \\ &\quad - \left(\frac{1}{2\Delta\xi_i (\Delta\xi_i + \Delta\xi_{i+1})} + \frac{1}{2\Delta\xi_i (\Delta\xi_i + \Delta\xi_{i-1})} \right) T_{f,i} \end{aligned} \quad (61)$$

405

The heat convection term in the fracture (Eq. 59) is approximated by

$$\begin{aligned} \left. \frac{w_f^2}{12\mu} \frac{\partial p_f}{\partial \xi} \frac{\partial T_f}{\partial \xi} \right|_i &= \frac{w_{f,i+1/2}^2}{12\mu} \frac{\partial p_{f,i+1/2}}{\partial \xi} T_{f,i+1/2} - \frac{w_{f,i-1/2}^2}{12\mu} \frac{\partial p_{f,i-1/2}}{\partial \xi} T_{f,i-1/2} \\ &= \frac{(w_{f,i} + w_{f,i+1})^2 (p_{f,i+1} - p_{f,i})}{48\mu (\Delta\xi_i + \Delta\xi_{i+1})} T_{f,i+1} - \frac{(w_{f,i} + w_{f,i-1})^2 (p_{f,i} - p_{f,i-1})}{48\mu (\Delta\xi_i + \Delta\xi_{i-1})} T_{f,i-1} \\ &\quad + \left(\frac{(w_{f,i} + w_{f,i+1})^2 (p_{f,i+1} - p_{f,i})}{48\mu (\Delta\xi_i + \Delta\xi_{i+1})} - \frac{(w_{f,i} + w_{f,i-1})^2 (p_{f,i} - p_{f,i-1})}{48\mu (\Delta\xi_i + \Delta\xi_{i-1})} \right) T_{f,i} \end{aligned} \quad (62)$$

Finally, the matrix form of the temperature field is expressed as

$$\begin{bmatrix} \mathbf{D}_m + \mathbf{U}_m + \mathbf{L}_{mf} & -\mathbf{L}_{mf} \\ -\mathbf{L}_{fm} & \mathbf{D}_f + \mathbf{U}_f + \mathbf{Y}_f + \mathbf{L}_{fm} \end{bmatrix} \begin{bmatrix} \mathbf{T}_m^{k+1} \\ \mathbf{T}_f^{k+1} \end{bmatrix} = \begin{bmatrix} \mathbf{F}_T \\ 0 \end{bmatrix} \quad (63)$$

where \mathbf{T}_m^{k+1} and \mathbf{T}_f^{k+1} are the vectors of temperature values in the matrix and fracture. \mathbf{U}_m and \mathbf{U}_f are the coefficient matrixes of heat conduction in the matrix and fracture derived from Equations (60) and (61). \mathbf{Y}_f is the coefficient matrix of heat convection in the fracture from Equation (62). The expressions of other sub-matrixes \mathbf{D}_m , \mathbf{D}_f , \mathbf{L}_{mf} , \mathbf{L}_{fm} and \mathbf{F}_T are listed in Appendix B.

3.3. Iterative solution scheme

415 The fluid pressure, temperature and stress fields interplay with each other and they are iteratively determined by the fixed mean stress split method. After the determination of these fields, the cohesive crack model is used to check whether the fracture propagates or

not. For the crack propagation strategy, the method presented in Elguedj et al. (2007) is here adapted. When the crack propagates, all enrichments are retained and new enrichment functions and new subelements are added. The new enriched DOFs are simply chosen to be initially zero. Besides, the new stresses are only due to elastic strains and the internal variables are initialized to zero on Gaussian points of new subelements. The overall iterative procedure for modeling hydraulic fracture propagation with THEP coupling is shown in Algorithm 1.

Algorithm 1 The overall iterative procedure for hydraulic fracture propagation with THEP coupling

- 1: Start: $t = 0$, $n = 1$, fracture is extended by a fixed length dL ;
- 2: **while** $t < t_{max}$ **do**
- 3: $l = 1$;
- 4: Assume the time step $\Delta t^{(n+1,l)}$ and fluid pressure in fracture $\mathbf{p}_f^{(n+1,l)}$;
- 5: Solve the elasto-plastic equations of stress field (Eq. 41), and calculate fracture width $\mathbf{w}_f^{(n+1,l)}$;
- 6: **while** $l < l_{max}$ **do**
- 7: Based on fracture width $\mathbf{w}_f^{(n+1,l)}$, solve the coupled equations of pressure field and temperature field iteratively:
- 8: $k = 1$, $\mathbf{p}_m^k = \mathbf{p}_m^{n+1,l}$, $\mathbf{p}_f^k = \mathbf{p}_f^{n+1,l}$, $\mathbf{T}_m^k = \mathbf{T}_m^{n+1,l}$, $\mathbf{T}_f^k = \mathbf{T}_f^{n+1,l}$;
- 9: **while** $k < k_{max}$ **do**
- 10: Solve the equations of pressure field (Eq. 57);
- 11: Solve global conservation equation (Eq. 29) to obtain new time step $\Delta t^{(n+1,l+1)}$;
- 12: Solve the equations of temperature field (Eq. 63);
- 13: Calculate the relative errors of variables between iteration k and $k + 1$:
- 14: $e_1 = \frac{|\mathbf{p}_m^{k+1} - \mathbf{p}_m^k|}{|\mathbf{p}_m^{k+1}|}$, $e_2 = \frac{|\mathbf{p}_f^{k+1} - \mathbf{p}_f^k|}{|\mathbf{p}_f^{k+1}|}$, $e_3 = \frac{|\mathbf{T}_m^{k+1} - \mathbf{T}_m^k|}{|\mathbf{T}_m^{k+1}|}$, $e_4 = \frac{|\mathbf{T}_f^{k+1} - \mathbf{T}_f^k|}{|\mathbf{T}_f^{k+1}|}$
- 15: **if** All the relative errors are smaller than tolerances **then**
- 16: $\mathbf{p}_m^{n+1,l+1} = \mathbf{p}_m^{k+1}$, $\mathbf{p}_f^{n+1,l+1} = \mathbf{p}_f^{k+1}$;
- 17: $\mathbf{T}_m^{n+1,l+1} = \mathbf{T}_m^{k+1}$, $\mathbf{T}_f^{n+1,l+1} = \mathbf{T}_f^{k+1}$;
- 18: **else** Jump out of this loop;

19: **end if**

20: $k = k + 1$;

21: **end while**

450 22: Based on new values of fluid pressure and temperature, solve the elasto-plastic equations of stress field (Eq. 41) to obtain displacement $\mathbf{u}^{(n+1,l+1)}$ and fracture width $\mathbf{w}_f^{(n+1,l+1/2)}$;

23: Calculate the relative errors of variables between iteration l and $l + 1$:

24:
$$e_1 = \frac{|\mathbf{p}_m^{(n+1,l+1)} - \mathbf{p}_m^{(n+1,l)}|}{|\mathbf{p}_m^{(n+1,l+1)}|}, e_2 = \frac{|\mathbf{p}_f^{(n+1,l+1)} - \mathbf{p}_f^{(n+1,l)}|}{|\mathbf{p}_f^{(n+1,l+1)}|}, e_3 = \frac{|\mathbf{T}_m^{(n+1,l+1)} - \mathbf{T}_m^{(n+1,l)}|}{|\mathbf{T}_m^{(n+1,l+1)}|}, e_4 = \frac{|\mathbf{T}_f^{(n+1,l+1)} - \mathbf{T}_f^{(n+1,l)}|}{|\mathbf{T}_f^{(n+1,l+1)}|},$$

455
$$e_5 = \frac{|\mathbf{u}^{(n+1,l+1)} - \mathbf{u}^{(n+1,l)}|}{|\mathbf{u}^{(n+1,l+1)}|}, e_6 = \frac{|\Delta t^{(n+1,l+1)} - \Delta t^{(n+1,l)}|}{|\Delta t^{(n+1,l+1)}|}$$

25: **if** All the relative errors are smaller than tolerances **then**

26: $t = t + \Delta t^{(n+1,l+1)}$, jump out of this loop;

27: **else**

28: $\mathbf{w}_f^{(n+1,l+1)} = \chi \mathbf{w}_f^{(n+1,l+1/2)} + (1 - \chi) \mathbf{w}_f^{(n+1,l)}$, ($0 < \chi < 0.5$);

460 29: **end if**

30: $l = l + 1$;

31: **end while**

32: Calculate the cohesive traction and energy release rate at fracture tip;

33: **if** Energy release rate exceeds the cohesive fracture energy σ_c **then**

465 34: Fracture is extended perpendicular to the maximum hoop stress direction;

35: **else**

36: Restart this loop;

37: **end if**

38: **end while**

470 4. Numerical results and discussions

In this section, we present the assessment of the proposed model and analysis of the effects of plastic deformation and heat transfer on hydraulic fracturing process.

4.1. Model assessment

4.1.1. Mandel's problem

475 Mandel's problem is well known for hydro-mechanical coupling, and it has been widely used as a benchmark case for evaluating numerical solutions for poro-elastic problems through comparisons with analytical solutions (Mandel, 1953). It is described as follows. A rectangular porous medium is sandwiched with two rigid, frictionless and impermeable plates. The medium is saturated with fluid, and the fluid is allowed to flow freely laterally. 480 An instantaneous force $2F$ is applied at the top and bottom boundaries. The lateral boundaries are traction free and exposed to atmospheric pressure (assumed to be zero). Due to the symmetry of problem, only a quarter of the domain is considered and shown in Figure 3.

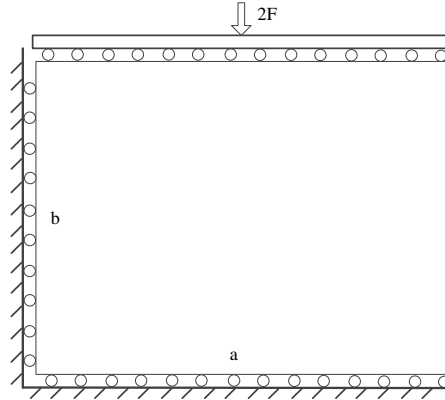


Figure 3: Quarter geometry and boundary conditions of Mandel's problem

According to Abousleiman et al. (1996), the analytical solutions of the y displacement 485 and the pore pressure are given as follows.

$$u_y = \left[-\frac{F(1-v)}{2Ga} + \frac{F(1-v)}{2Ga} \sum_{i=1}^{\infty} \frac{\sin \beta_i \cos \beta_i}{\beta_i - \sin \beta_i \cos \beta_i} \exp(-\beta_i^2 c_d t / a^2) \right] y \quad (64)$$

$$p = \frac{2FB(1+v_u)}{3a} \sum_{i=1}^{\infty} \frac{\sin \beta_i}{\beta_i - \sin \beta_i \cos \beta_i} \left(\cos \frac{\beta_i x}{a} - \cos \beta_i \right) \exp(-\beta_i^2 c_d t / a^2) \quad (65)$$

where a is the length of the rectangle, and F is half of the applied force. G and v are the shear modulus and Poisson's ratio. B is the Skempton pore pressure coefficient. v_u is the

undrained Poisson's ratio. c_d is the diffusivity coefficient. Their expressions are listed as follows.

$$B = 1 - \frac{\phi_m K_d (K_s - K_f)}{K_f (K_s - K_d) + \phi_m K_d (K_s - K_f)} \quad (66)$$

$$v_u = \frac{3v + B(1 - 2v)(1 - K_d/K_s)}{3 - B(1 - 2v)(1 - K_d/K_s)} \quad (67)$$

$$c_d = \frac{2k_m B^2 G(1 - v)(1 + v_u)^2}{9\mu_f(1 - v_u)(v_u - v)} \quad (68)$$

490 where K_d , K_s and K_f are, respectively, the bulk modulus of the solid skeleton, the solid constituent and the fluid. ϕ_m is the porosity of medium. Besides, in the above relations (Eqs. 64, 65), β_i satisfies the following equation

$$\tan \beta_i = \frac{1 - v}{v_u - v} \beta_i \quad (69)$$

We take the y displacement at the top calculated from Equation (64) as displacement boundary condition and compute the pore pressure to compare with the analytical solution 495 (Eq. 65). The hydro-mechanical coupling is solved by the fixed mean stress split scheme as presented in the numerical algorithm section. The rock and fluid parameters are listed in Table 1. The comparison result of normalized pore pressure versus normalized distance is shown in Figure 4. It shows that the numerical solutions of the normalized pore pressure agree well with the analytical solutions at different time steps. The result shows good 500 accuracy of the hydro-elastic part of our numerical code.

Table 1: Rock and fluid parameters used for Mandel's problem

Parameter	Magnitude	Unit
Length a	100	m
Width b	10	m
Young's modulus E	5	GPa
Poisson's ratio ν	0.25	-
Biot's coefficient α	0.9	-
Biot's modulus M	11.4	GPa
Drained modulus K_d	3.33	GPa
Modulus of solid constituent K_s	33.3	GPa
Modulus of fluid K_f	3	GPa
Permeability k_m	0.1	D
Porosity ϕ_m	0.2	-
Fluid viscosity μ	1	mPa · s

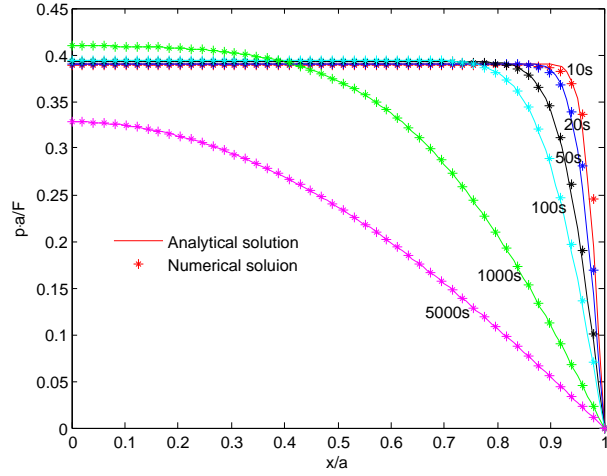


Figure 4: Comparison of normalized pore pressure between analytical and numerical solutions

It should be noted that the rock deformation is elastic in Mandel's problem. Further, we extend the poroelasticity (elastic model) to poroplasticity (plastic model) for studying the

effect of rock plasticity on pressure variation by assuming the same displacement boundary values at the top surface (Eq. 64). The input parameters for the elastic model are the same as the ones in Table 1. Other rock plastic parameters for the plastic model are described as follows. The rock is assumed to be a perfect elastic-plastic material. The cohesion and internal friction angle are, respectively, set to be 10^5 Pa and 35° . The comparison result of normalized pore pressure versus normalized distance between the elastic model and plastic model is shown in Figure 5. It is observed that the initial (short term) rise of pore pressure is nearly the same in the elastic model and plastic model. As the fluid flows in time, the pore pressure becomes smaller in the plastic model than that in the elastic model.

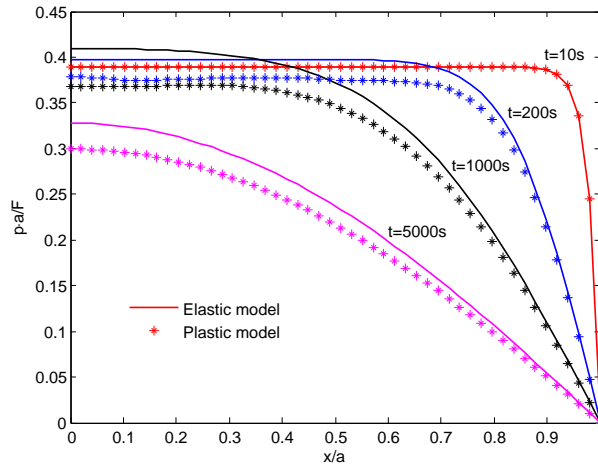


Figure 5: Comparison result of pore pressure between elastic and plastic models

In order to see the pore pressure evolution over time, three points are selected as the observation points at the bottom surface with normalized distance as 0, 0.38 and 0.7. The pore pressure evolution is plotted in Figure 6 for the elastic model and plastic model. It can be observed that after an initial instantaneous rise, the pore pressure near the central region increases firstly and then decreases in the elastic model, which is known as the Mandel-Cryer effect (Cryer, 1963). This region is called the Mandel-Cryer zone. However, it is interesting to see that the Mandel-Cryer effect is not observed or significantly attenuated in the plastic model. This is due to the fact that the Mandel-Cryer zone observed in the elastic model is subjected to plastic volumetric dilatancy, producing a weak effect on pore fluid pressure

rise.

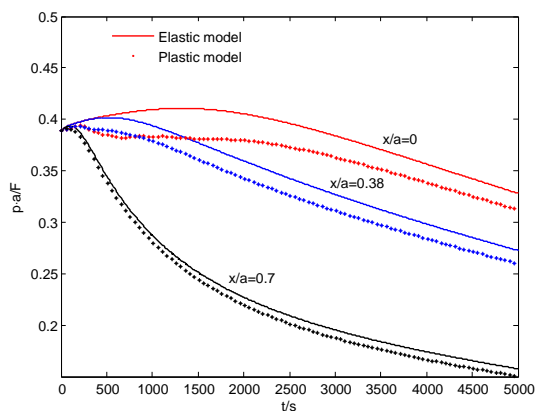


Figure 6: Comparison result of pore pressure evolution between the elastic model and plastic model

4.1.2. Poro-elastic model in fractured media

As previously mentioned in the introduction, (Réthoré et al., 2007b) presented a two-scale approach for coupled fluid flow and mechanical problem in fractured porous media.

525 To demonstrate the efficiency of the coupling method of XFEM and EDFM proposed in this study, the same case presented in (Réthoré et al., 2007b) is here solved by using the XFEM-EDFM coupling method. In that considered problem, an inclined fracture (2 m long) is centered in the specimen (10 m \times 10 m), as shown in Figure 7. The same boundary conditions and input parameters as those in (Réthoré et al., 2007b) are used. The bottom
530 side is assigned a normal fluid flux $q_0 = 10^{-4}$ m/s while the top side is assigned a constant pressure of zero. Both the left and right sides are assigned undrained conditions. The input parameters are set with Young's modulus $E = 9$ GPa, Poisson ratio $\nu = 0.4$, Biot's coefficient $\alpha = 1$, Biot's modulus $M = 10^{18}$ GPa, matrix permeability $k_m = 10^{-9}$ m², and fluid viscosity $\mu = 10^{-3}$ mPa \cdot s.

535 To compare the results between the present study and Rethore's study, the ratios of outward flow over influx for the fracture inclined angles of 30° and 45° are calculated, and the comparison results are shown in Figure 8. It can be seen that there is a good agreement between the two studies. The predicted values by the present study are slightly larger than those in Rethore's one. The reason for this may be that we presume a small value for

540 residual fracture width in the EDFM solution of fluid flow. The y displacement distribution in the specimen is also plotted in Figure 9, from which one can see a similar distribution and range of displacement as those shown in Réthoré et al. (2007b). Therefore, it seems that the XFEM-EDFM coupling method is efficient for solving poro-elastic modeling in the fractured porous media.

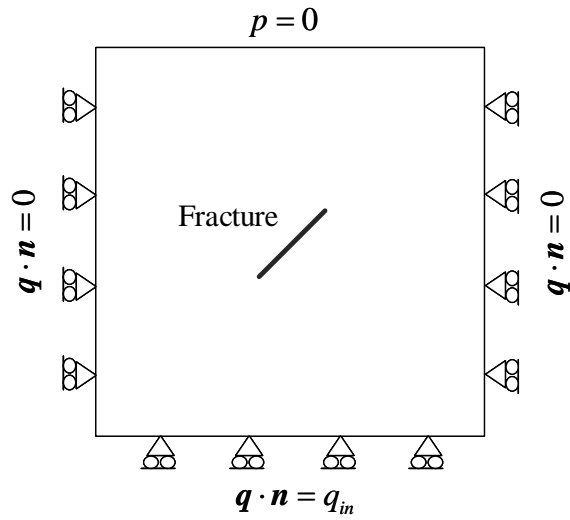


Figure 7: Schematic presentation of fractured specimen with boundary conditions

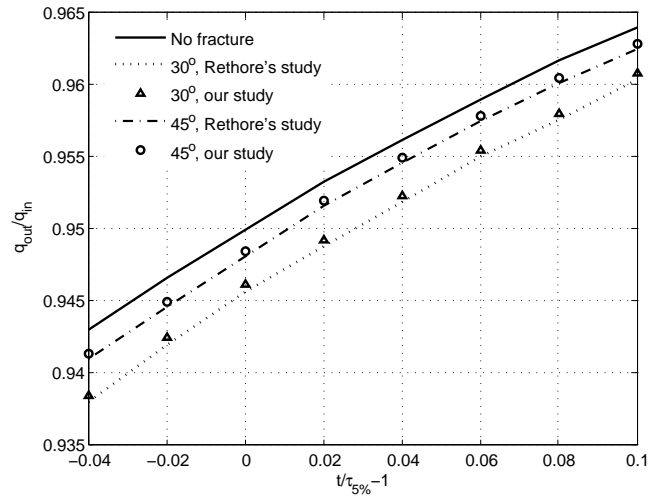


Figure 8: Comparison of ratio of outward flow over influx between two studies

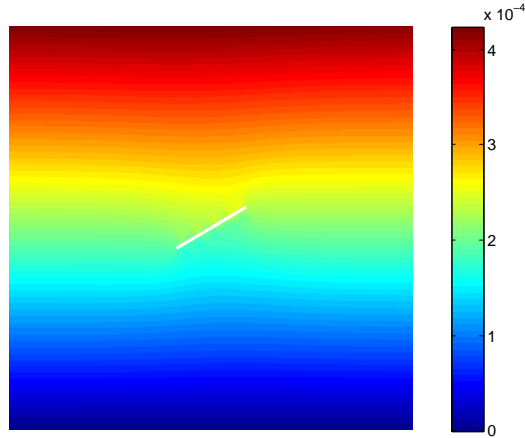


Figure 9: Contour of y displacement for fracture inclination angle of 30°

545 *4.1.3. Thermo-hydraulic problem*

In this study, the heat transfer in the medium with a fracture is solved by the embedded discrete fracture model (EDFM), which was initially developed for fluid flow problem. To validate the application of EDFM to heat transfer problem, a simple case is studied. Just like hydraulic fracturing, a fracture with a constant width $2d_f$ is placed at the center of the domain. Fluid is injected from the inlet at the constant temperature T_{inlet} and constant velocity v_l . The rock is assumed to be isotropic and impermeable with an initial uniform temperature T_{initial} . The geometry of the model is illustrated in Figure 10.

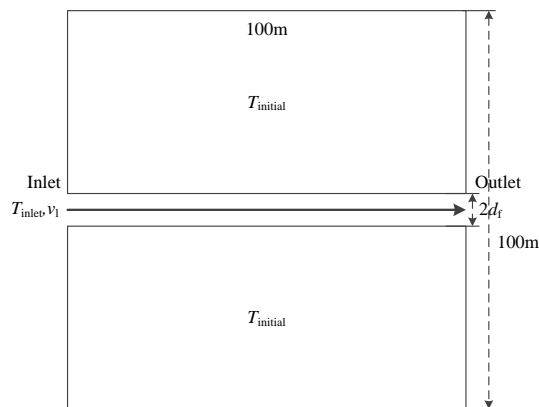


Figure 10: Geometry of the thermo-hydraulic problem

The analytical solution of the temperature in the fracture for this case can be found in

Barends (2010), that is

$$T(x, t) = T_{\text{initial}} + (T_{\text{inlet}} - T_{\text{initial}}) \operatorname{erfc} \left(\frac{\lambda_s x}{2\rho_f c_f d_f \sqrt{\lambda_s v_l (v_l t - x) / (\rho_s c_s)}} \right) U \left(t - \frac{x}{v_l} \right) \quad (70)$$

555 where erfc is the complementary error function, and U is the unit step function.

The rock and fluid parameters for the case are given in Table 2. The analytical solutions (Eq. 70) and the numerical results are computed and presented for comparison. The temperature distribution in the fracture at different time steps are shown in Figure 11, and the temperature evolution over time at three selected points ($x = 11$ m, 21 m and 50 m) 560 are plotted in Figure 12. It can be seen that the numerical results by using EDFM are in good agreement with the analytical solutions. Hence the proposed numerical method for thermo-hydraulic part is verified.

Table 2: Rock and fluid parameters used for thermo-hydraulic problem

Parameter	Magnitude	Unit
Rock density ρ_s	2700	kg/m ³
Fluid density ρ_f	1000	kg/m ³
Rock heat capacity c_s	1000	J/(kg · K)
Fluid heat capacity c_f	4200	J/(kg · K)
Rock thermal conductivity λ_s	3	W/(m · K)
Fluid thermal conductivity λ_f	0.6	W/(m · K)
Fluid velocity v_l	0.01	m/s
Fracture half-width d_f	0.0005	m
Heat transfer coefficient h_t	20	W/(m ² · K)
Initial temperature T_{initial}	80	°C
Inlet temperature T_{inlet}	20	°C

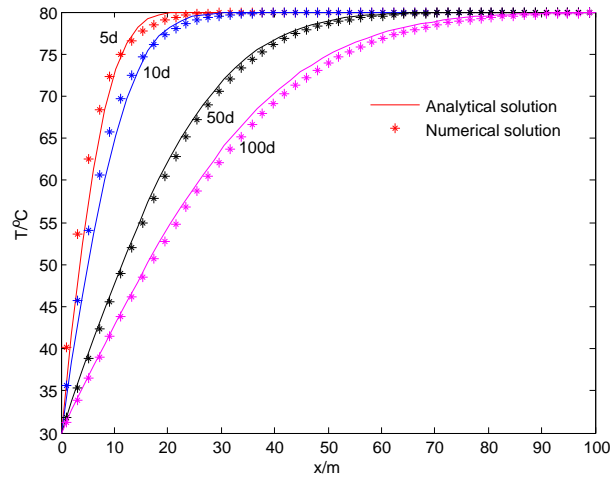


Figure 11: The analytical and numerical results of temperature distribution in the fracture

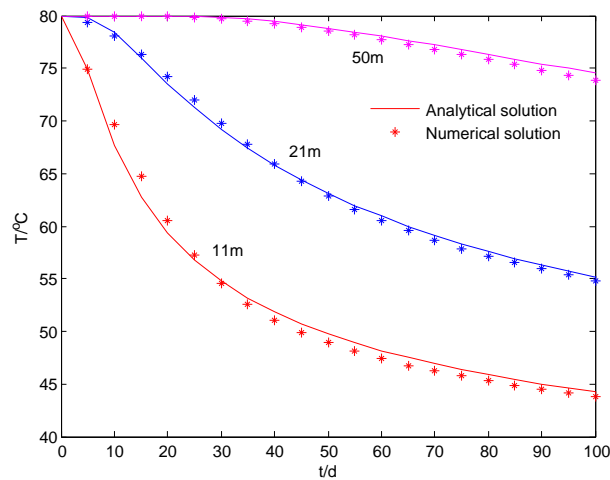


Figure 12: The analytical and numerical results of temperature evolution over time

4.1.4. KGD fracture model

The last part of the model assessment is the crack propagation process. KGD model is widely used for testing and verifying numerical solutions for hydraulic fracture propagation (Khristianovic and Zheltov, 1955; Geertsma and Klerk, 1969). A fracture is initiated from the injection point and allowed to propagate in an infinite material domain under plane strain condition. Due to the symmetry, only a half of the geometrical domain is considered as shown in Figure 13.

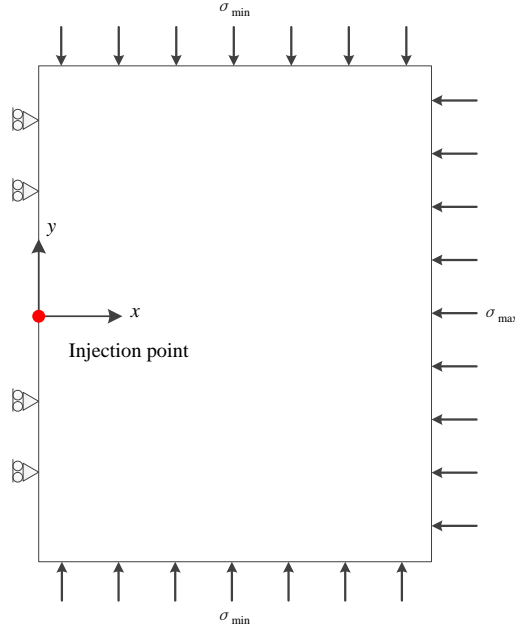


Figure 13: Geometry configuration and boundary conditions of KGD model

570 According to Valko and Economides (1995), the analytical solutions of the evolution of fracture half length, fracture width and net pressure over time are given as follows.

$$L(t) = 0.539 \left(\frac{E' Q_0^3}{\mu} \right)^{1/6} t^{2/3} \quad (71)$$

$$w_w(t) = 2.36 \left(\frac{\mu Q_0^3}{E'} \right)^{1/6} t^{1/3} \quad (72)$$

$$p_{n,w} = 1.09 (E'^2 \mu)^{1/3} t^{-1/3} \quad (73)$$

where E' is the plane strain modulus, and Q_0 is the injection flow rate.

The used values of rock and fluid parameters are listed in Table 3. The calculated results of fracture half length for three values of Young's modulus are compared and plotted in Figure 14. In addition, the analytical and numerical solutions of the fracture width and net pressure at the injection point are shown in Figure 15 and 16. It can be seen that the analytical solutions and numerical results are in good concordance for all considered cases, which verifies the numerical method proposed for crack propagation in this study.

Table 3: Rock and fluid parameters used for KGD fracture model

Parameter	Magnitude	Unit
Young's modulus E	30	GPa
Poisson's ratio ν	0.25	-
Cohesive strength σ_c	0.4	MPa
Cohesive fracture energy G_c	100	Pa · m
Permeability k_m	0	D
Fluid viscosity μ	1	mPa · s
Injection rate Q_0	0.0001	m ³ /s

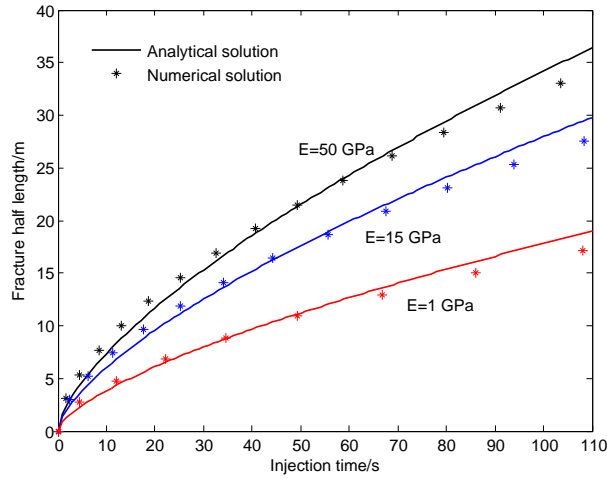


Figure 14: The analytical and numerical solutions of fracture half length for different moduli

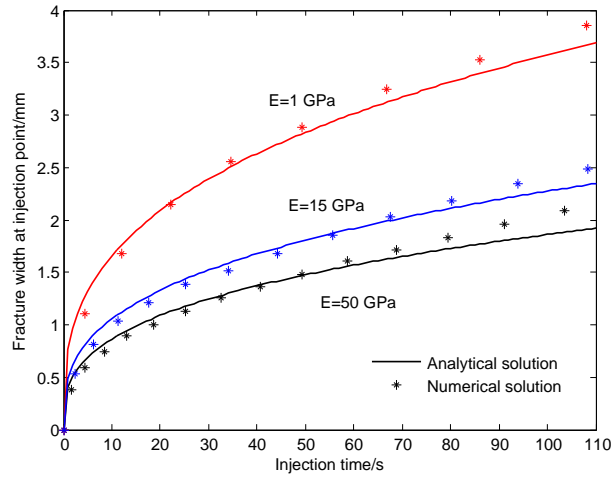


Figure 15: The analytical and numerical solutions of fracture width at the injection point for different moduli

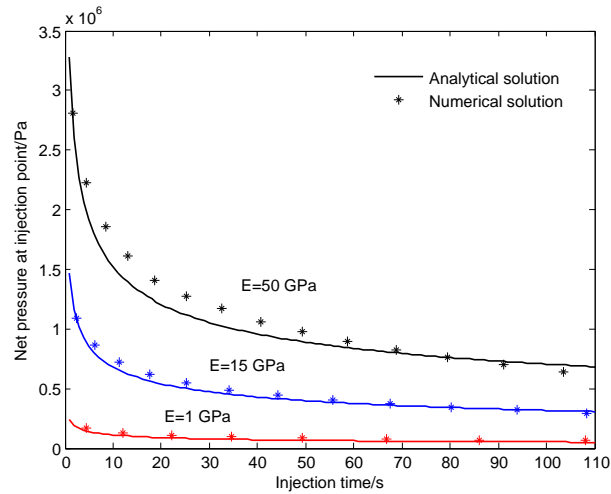


Figure 16: The analytical and numerical solutions of net pressure at the injection point for different moduli

4.2. Effect of plastic deformation

580 In this section, we analyze the effect of rock plastic deformation on hydraulic fracturing process without consideration of thermal effect. There are several parameters involved in plastic deformation, such as cohesion, internal friction angle and hardening exponent. Without intension of making an exhaustive sensitivity study of all parameters, only the cohesion is selected as an influencing factor of plastic deformation on hydraulic fracture propagation.

585 To this end, the rock and fluid parameters are kept unchanged and listed in Table 4, expect the cohesion which is set as 1 MPa, 3 MPa, 5 MPa and 10 MPa.

Table 4: Rock and fluid parameters used for plastic fracture model

Parameter	Magnitude	Unit
Young's modulus E	20	GPa
Poisson's ratio ν	0.2	-
Internal friction angle ϕ	30	deg
Hardening parameter H_v	10^4	Pa
Cohesive strength σ_c	0.5	MPa
Cohesive fracture energy G_c	50	Pa · m
Biot's coefficient α	0.9	-
Biot's modulus M	41.1	GPa
Permeability k_m	0.1	mD
Porosity ϕ_m	0.05	-
Fluid viscosity μ	10	mPa · s
Injection rate Q_0	0.0005	m ³ /s

The geometrical model is a square with 50 m × 50 m, and it is meshed into 49 × 49 square elements. In Figure 17, one shows the variation of fracture half length obtained with different values of rock cohesion. Correspondingly, in Figures 18 and 19, we present the variation of fracture width and fluid pressure at the injection point over time. It can be seen from these results that at a given injection time, as the cohesion decreases the fracture half length increases whereas the fracture width and fluid pressure increase. It is indicated that the plastic deformation reduces the fracture propagation velocity but enhances the propagating pressure of a hydraulic fracture.

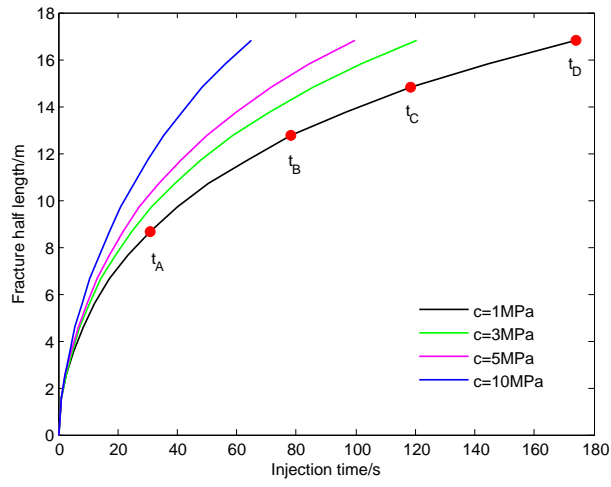


Figure 17: Variations of fracture half length solved with using different values of rock cohesion

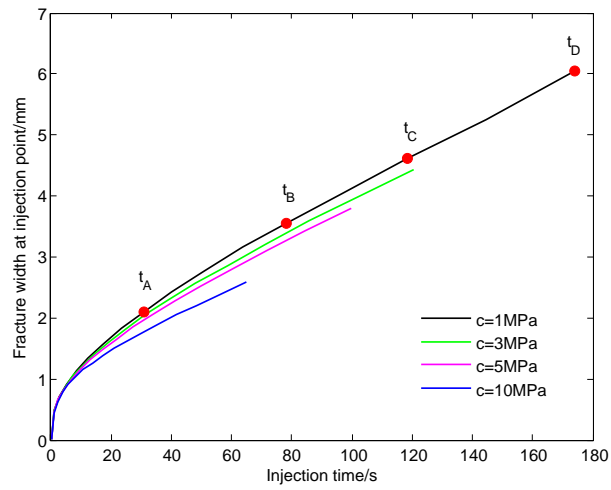


Figure 18: Variations of fracture width at the injection point solved with using different values of rock cohesion

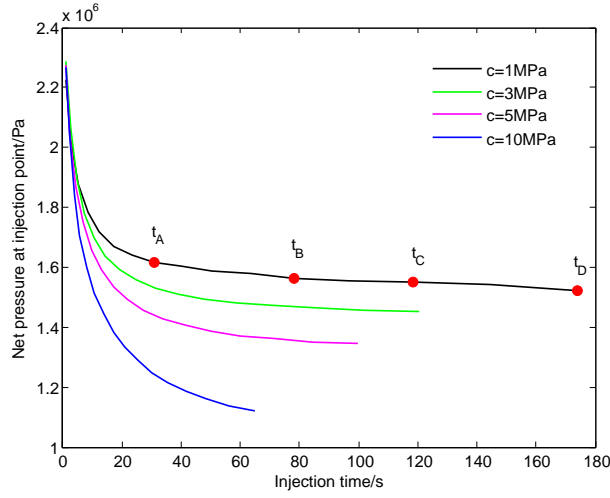


Figure 19: Variations of fluid pressure at the injection point with different values of rock cohesion

595 In order to give a more detailed view on the process of hydraulic fracture propagation, the contour results of several key quantities are presented at different injection time steps in the case with the minimum cohesion of 1 MPa. These different time steps correspond to the red points indicated in Figures 17, 18 and 19. The first quantity is y displacement as shown in Figure 20. The white lines in this figure represent fractures, which have the same
600 meaning in the following contour Figures. In these Figures, the color bars are set to the same scale. It can be observed that a displacement jump exists across the fracture, that is the fracture width.

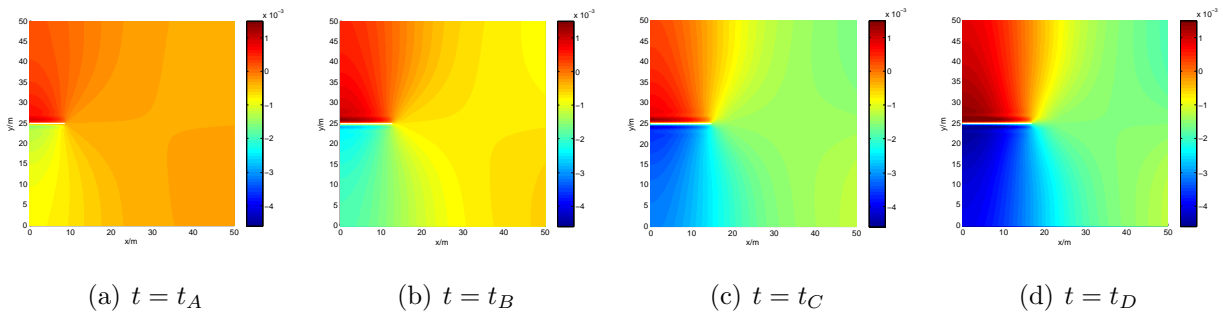


Figure 20: Contours of y displacement at different time steps

The contours of fluid pressure and Mises equivalent stress are respectively presented in Figure 21 and Figure 22. One can see that as the fracture propagates towards,

605 from the fracture into the matrix, and the pore pressure rises in the region at the upper and lower surfaces of fracture whereas it drops in the front of fracture tip. In addition, as the fracture extends towards, Mises equivalent stress increases in the medium especially in front of fracture tip. Even though Drucker-Prager yield criterion is adopted in this study, Mises equivalent stress can still serve as an indicator of plastic deformation level. One observes
610 that the plastic deformation mainly occurs around the fracture.

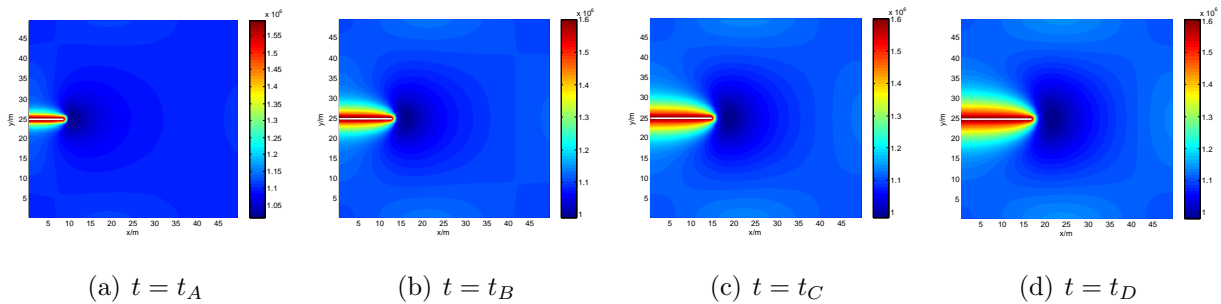


Figure 21: Contours of fluid pressure at different time steps

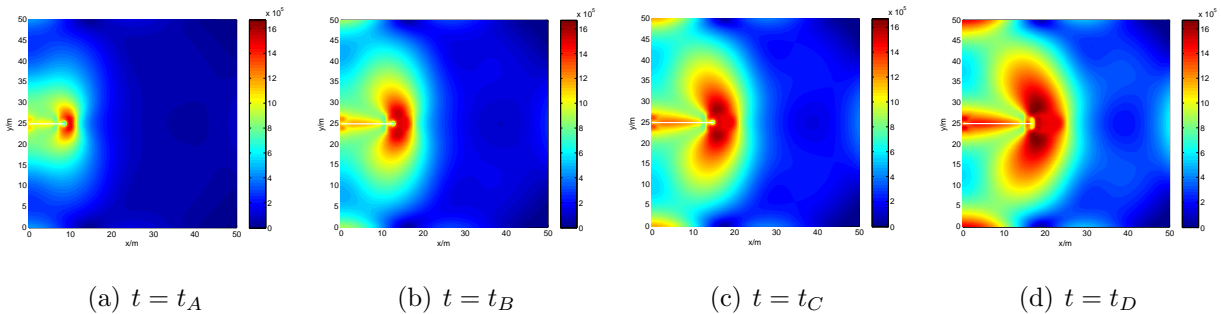


Figure 22: Contours of Mises stress at different time steps

The last quantity considered is the accumulated plastic strain as shown in Figure 23. The color bars are also set to the same scale to see the time evolution of the accumulated plastic strain. It is shown that the accumulated plastic strain is nonzero in the grid around the fracture, in agreement with the distribution of Mises equivalent stress. As the fracture
615 propagates, the accumulated plastic strain increases. As the plastic strain is irreversible, when the injection stops and fluid flows back, the fracture will remain open with a residual

width even if there are no proppants inside the fracture. And the residual width of fracture depends on the accumulated plastic strain. The larger accumulated plastic strain is, the wider fracture residual width is.

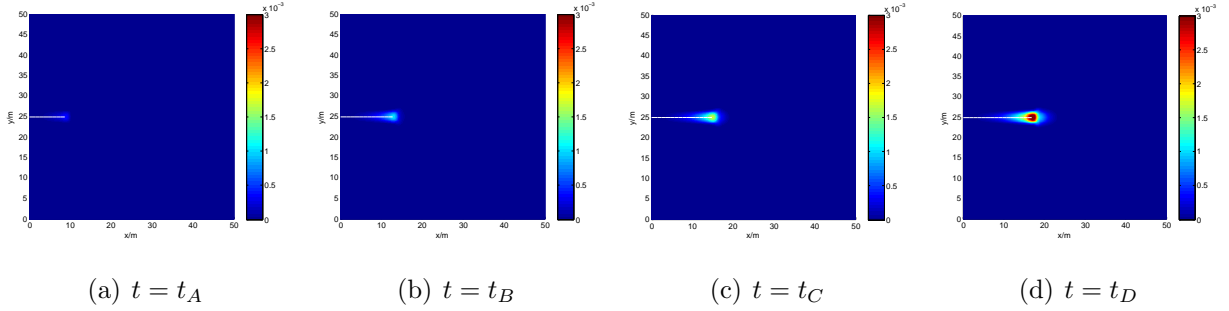


Figure 23: Contours of accumulated plastic strain at different times

620 There is only one fracture in the above cases. As an additional example, one considers now two hydraulic fractures propagating simultaneously. The geometrical model is illustrated in Figure 24. Two fractures are assumed to initiate from the left boundary of domain, and the injection rates are the same for both of them. The fracture propagation paths and accumulated equivalent plastic strain are shown in Figure 24. One can see that the fractures
625 deflect from their initial directions and extend outwards from each other due to the effect of stress redistributions around the fractures. Further, we also analyze the effect of mesh size on the propagation paths of hydraulic fractures. The domain has an area of $50 \text{ m} \times 50 \text{ m}$. The domain is discretized into quadrilateral elements with a number of 200×200 in the above case. A coarser (100×100) and a finer mesh (250×250) are used in the additional
630 calculations. The fracture propagation paths obtained with the three types of meshes are shown in Figure 25. A little difference of predicted fracture propagation paths is obtained between the different meshes. This indicates that the proposed numerical model has a small mesh dependency and the mesh used in the examples above is sufficiently refined.

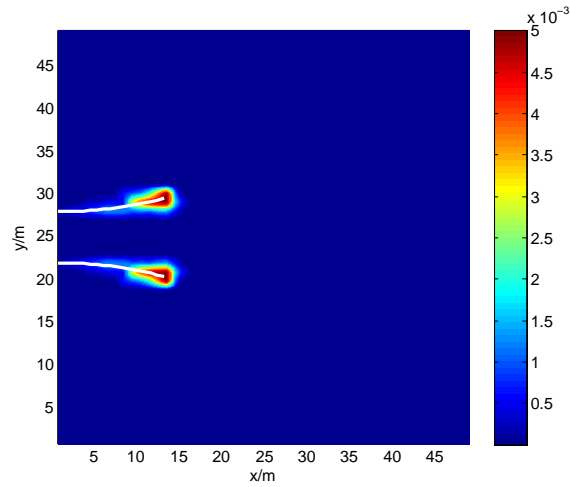


Figure 24: Contour of accumulated equivalent plastic strain after 60s injection (the white lines represent fractures)

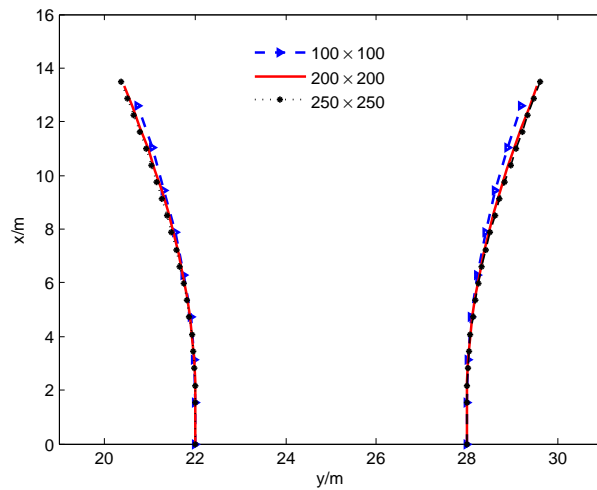


Figure 25: Fracture propagation paths obtained by using different element numbers

On the other hand, in Figure 26, we compare the fracture propagation paths obtained by
 635 our model for both the elastic and plastic materials. For the sake of a clear illustration, the
 x axis and y axis are rotated. Moreover, this kind of problems for two hydraulic fractures
 propagation under elastic conditions have been studied by using various numerical methods,
 for instance the displacement discontinuity method (Wu et al., 2015). Thus, in order to
 have a comparison with other methods, we have performed a new calculation by using the

640 DDM in the elastic case and the obtained fracture paths are given in the same Figure. The fracture paths predicted by our elastic model are well consistent with those by DDM, which verifies the accuracy of the proposed model for non-straight crack propagation problems. It is also found that when the plastic deformation is considered, the fracture lengths decrease, as already observed in the previous cases. An interesting phenomenon is that the plastic deformation also has an impact on the fracture propagation path. The deflection of fracture direction is enhanced by the plastic deformation in comparison with the elastic model. In other words, the effect of stress redistribution is enhanced when the plastic deformation is taken into account. The plastic deformation casts a significant influence not only on the fracture length but also on the fracture propagation path when multiple fractures propagate

645

650 simultaneously.

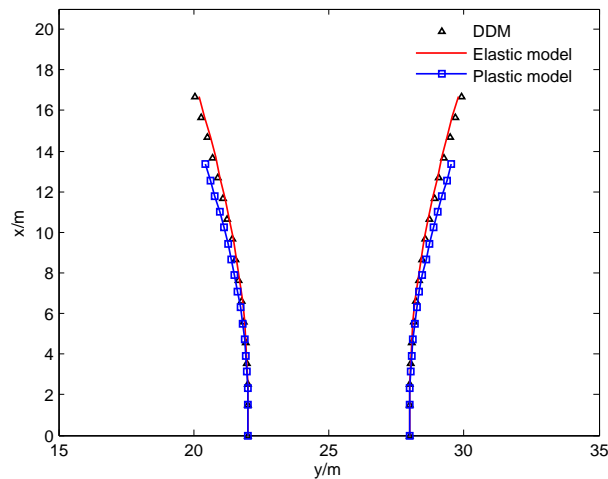


Figure 26: Comparison of fracture paths between the elastic model, plastic model and DDM solution

4.3. Effect of heat transfer

In this section, the combined effect of plastic deformation and heat transfer are considered in the modeling of hydraulic fracture propagation. The deep reservoir usually has an initial high temperature, which gives rise to the cooling effect when low temperature fluid is injected to initiate and extend a hydraulic fracture. To investigate the thermal effect on the hydraulic fracturing, the initial temperature of reservoir varies from 75° to 125° whereas the

655

temperature of injected fluid is fixed at 25° . In addition, a reference case is first studied by setting the initial temperature of reservoir equal to that of the injected fluid. Other inputs of rock and fluid parameters are the same as those for the plastic fracture modeling as given in Table 4. The cohesion of rock is fixed at 3 MPa. And the thermo-physical parameters of rock and fluid, such as density, heat capacity and thermal conductivity, are the same as for the thermo-hydraulic modeling as given in Table 2 and presented in the section of model assessment. The coefficients of linear thermal expansion of fluid and solid (α_f, α_s) are set as 7×10^{-5} 1/K and 8×10^{-6} 1/K, and the thermal hardening coefficient H_t is zero.

A series of numerical calculations are performed with different values of initial reservoir temperature. Firstly, the variation of fracture half length is studied and shown in Figure 27. It is seen that as the initial reservoir temperature or equivalently the temperature difference between reservoir and injected fluid increases, the fracture half length decreases for a given injection time. This indicates that the cooling of reservoir temperature by fluid injection reduces the kinetics of hydraulic fracture propagation. In addition, in Figure 28, one can see that as the initial reservoir temperature increases, the fracture width tends to increase. It is interesting to observe that the fluid pressure decreases in this situation as shown in Figure 29. In general, a larger pressure is needed to obtain a wider fracture. However, this is not applicable when the cooling effect of heat transfer is taken into account. This is due to the fact that the cooling effect gives rise to extra tensile stress on the fracture surface.

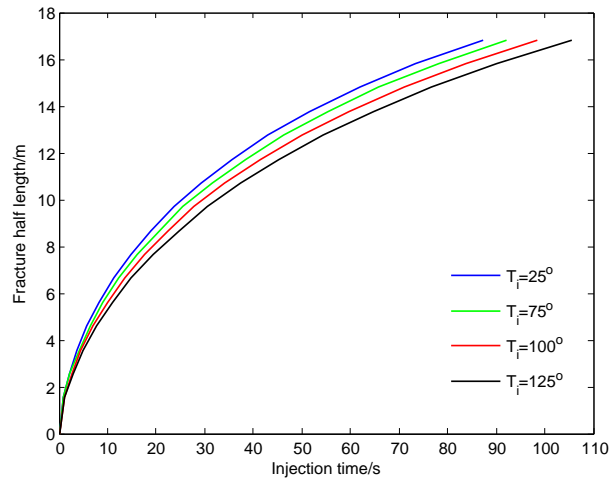


Figure 27: Variations of fracture half length solved with different initial temperatures of reservoir

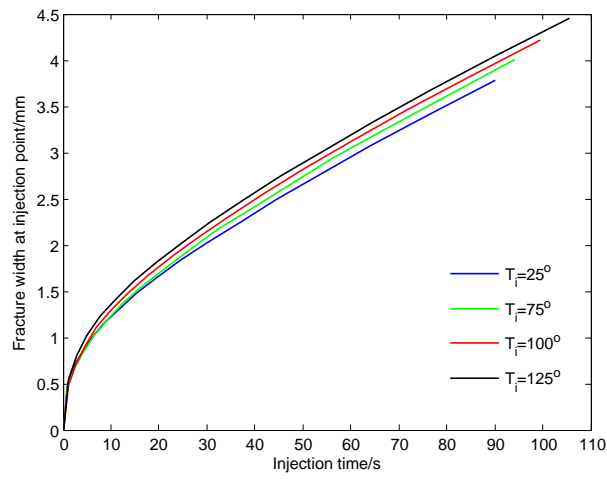


Figure 28: Variations of fracture width at the injection point solved with different initial temperatures of reservoir

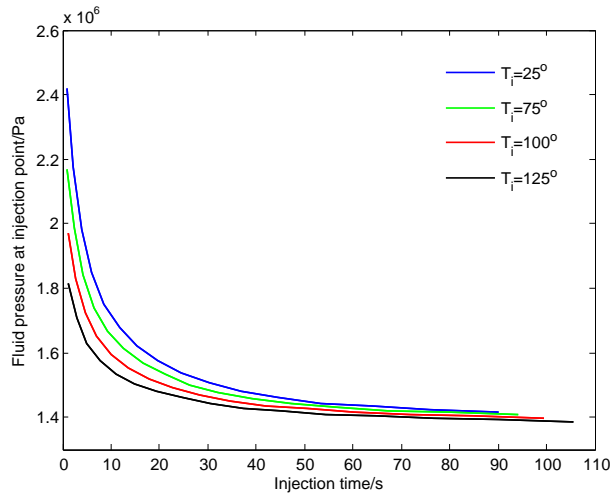


Figure 29: Variations of fluid pressure at the injection point solved with different initial temperatures of reservoir

The fluid temperature in the fracture is also obtained and shown in Figure 30. When the reservoir temperature is the same as that of injected fluid, there is no heat transfer between two systems. Hence there is no change of temperature of fluid in the fracture. When the initial reservoir temperature is higher than that of injected fluid, the fluid is heated and gradually approaches to the temperature of reservoir. This is significant for developing enhanced geothermal systems by means of hydraulic fracturing. Meanwhile, the reservoir gets cooled and the matrix contraction is induced around the fracture.

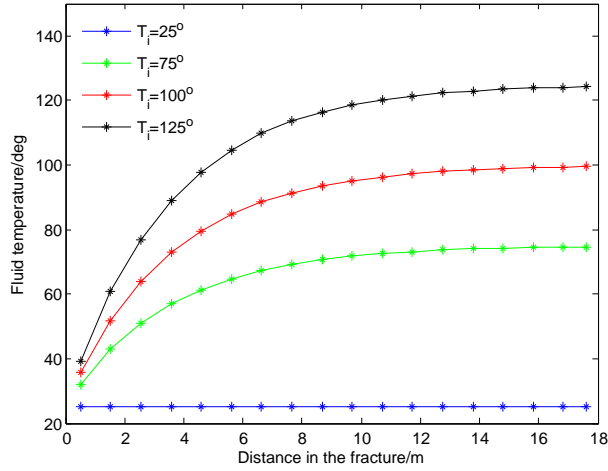


Figure 30: Variation of fluid temperature in the fracture obtained with different values of initial reservoir temperature

As the reservoir gets cooled, the temperature increment becomes negative near the fracture. The plastic deformation of rock is closely related to the temperature variation. It is then useful to investigate the thermal effect on plastic deformation of rock. A series of calculations are performed with different values of initial reservoir temperature. The maximum accumulated plastic strain is presented in Figure 31. We can see that when the initial reservoir temperature is higher than that of injected fluid, the accumulated plastic strain falls below that of the case in which the initial reservoir temperature is the same as the injected fluid. Moreover, as the temperature difference between reservoir and fluid increases, the diminution of accumulated plastic strain is amplified. It indicates that the cooling of rock has an effect of decreasing the plastic deformation.

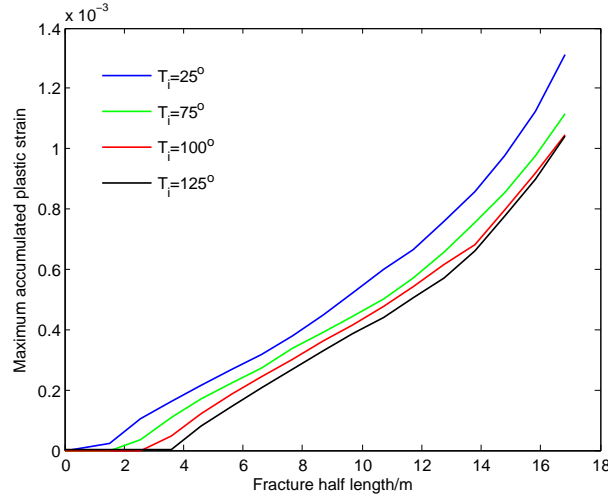


Figure 31: Variation of maximum accumulated plastic strain with different values of initial reservoir temperature

5. Concluding remarks

We have presented a coupled thermo-hydro-elastic-plastic model for the study of hydraulic fracturing in saturated porous media. A combined EDFM-XFEM approach has been developed. Based on the fixed mean stress split scheme, the overall solution procedure has been well established, coupling three physical fields as well as the crack propagation process. The proposed approach is validated against analytical solutions for several well-established cases. The coupled effect of plastic deformation and heat transfer on hydraulic fracturing process has been addressed. In order to clearly emphasize this effect, we have considered in this study only the case with the propagation of a single fracture. But the proposed numerical method is able to deal with those cases with multiple fractures.

The obtained results show that the plastic yielding occurs mainly in the area around the fracture. The plastic deformation results in a rise of fracture propagation pressure and reduction of fracture propagation velocity. As the materials cohesion decreases, the accumulated plastic strain increases and the influence of plastic deformation on hydraulic fracture parameters is enhanced. It is also indicated that the plastic deformation has little influence on the fracture propagation direction. Moreover, the cooling of rock matrix due

to injecting cold fluid induces tensile thermal stress. This leads to a reduction of fracture
710 propagation pressure. The heat transfer has an opposite effect to that of plastic deformation
on the fracture propagation pressure. This implies that when the combined effect of plastic
deformation and heat transfer is considered, the fracture propagation pressure is balanced
by these two processes. The heat transfer also impacts the accumulated plastic strain.
Therefore, the hydraulic fracturing process is influenced by the complex interaction between
715 fluid flow, heat transfer and plastic deformation.

6. Acknowledgement

We acknowledge that this study is jointly supported by National Natural Science Founda-
tion of China (51904321, 51774317), National Science and Technology Major Project
of China (2016ZX05060-010), Fundamental Research Funds for the Central Universities
720 (18CX05029A).

Appendix A. Return mapping algorithm of plastic model with consideration of thermal effect

According to Equation (11), the plastic strain increment can be expressed by the plastic
flow vector.

$$d\boldsymbol{\varepsilon}^p = d\gamma \mathbf{X} \quad (\text{A.1})$$

$$\mathbf{X} = \frac{\partial f}{\partial \boldsymbol{\sigma}'} = \frac{1}{2\sqrt{J_2(\mathbf{s})}} \mathbf{s} + \eta \mathbf{I} \quad (\text{A.2})$$

The deviatoric/volumetric decomposition of the flow vector gives

$$\mathbf{X}_d = \frac{1}{2\sqrt{J_2(\mathbf{s})}} \mathbf{s} \quad (\text{A.3})$$

$$X_v = 3\eta \quad (\text{A.4})$$

According to Equation (12), the effective stress increment can be expressed as follows

$$d\boldsymbol{\sigma}' = \mathbf{C} : d\boldsymbol{\varepsilon} - \mathbf{C} : d\boldsymbol{\varepsilon}^p - 3\alpha_s K_D dT \mathbf{I} \quad (\text{A.5})$$

Therefore, the return mapping update formula for the stress tensor is written as

$$\boldsymbol{\sigma}'_{k+1} = \boldsymbol{\sigma}_{k+1}^{trial} - d\gamma \left[2G_D(\mathbf{X}_d)_{k+1} + K_D(X_v)_{k+1} \right] - 3\alpha_s K_D dT \mathbf{I} \quad (\text{A.6})$$

730 where $\boldsymbol{\sigma}_{k+1}^{trial}$ is the elastic trial stress.

Substituting Equations (A.3, A.4) into Equation (A.6) yields

$$\boldsymbol{\sigma}'_{k+1} = \boldsymbol{\sigma}_{k+1}^{trial} - d\gamma \left[\frac{G_D}{\sqrt{J_2(\mathbf{s}_{k+1})}} \mathbf{s}_{k+1} + 3K_D \bar{\eta} \mathbf{I} \right] - 3\alpha_s K_D dT \mathbf{I} \quad (\text{A.7})$$

Due to the definition of J_2 , the following identity holds

$$\frac{\mathbf{s}_{k+1}}{\sqrt{J_2(\mathbf{s}_{k+1})}} = \frac{\mathbf{s}_{k+1}^{trial}}{\sqrt{J_2(\mathbf{s}_{k+1}^{trial})}} \quad (\text{A.8})$$

Substituting Equation A.8 into stress update formula (A.7), the deviatoric and volumetric parts of stress can be updated as follows

$$\mathbf{s}_{k+1} = \left(1 - \frac{d\gamma G_D}{\sqrt{J_2(\mathbf{s}_{k+1}^{trial})}} \right) \mathbf{s}_{k+1}^{trial} \quad (\text{A.9})$$

735

$$I_{1,k+1} = I_{1,k+1}^{trial} - 9d\gamma K_D \eta - 9\alpha_s K_D dT \quad (\text{A.10})$$

The consistency condition at the present step is given by

$$f_{k+1} = \sqrt{J_2(\mathbf{s}_{k+1})} + \eta I_1(\boldsymbol{\sigma}'_{k+1}) - \zeta(\varepsilon_{v,k+1}^p, dT) = 0 \quad (\text{A.11})$$

The accumulative plastic volume strain is expressed by the plastic multiplier as follows

$$\varepsilon_{v,k+1}^p = \varepsilon_{v,k}^p + d\varepsilon_v^p = \varepsilon_{v,k}^p + 3\eta d\gamma \quad (\text{A.12})$$

Substituting Equations (A.9, A.10, A.12) into Equation (A.11) gives a nonlinear equation of the plastic multiplier.

$$f(d\gamma) = \sqrt{J_2(\mathbf{s}_{k+1}^{trial})} - d\gamma G_D + \eta(I_{1,k+1}^{trial} - 9d\gamma K_D \eta - 9\alpha_s K_D dT) - \zeta(\varepsilon_{v,k}^p + 3\eta d\gamma, dT) = 0 \quad (\text{A.13})$$

740

After iteratively solving the above nonlinear equation (A.13) and obtaining the plastic multiplier $d\gamma$, the stress can be updated according to Equations (A.9, A.10).

Since the plastic flow vector is not defined at the apex of the Drucker-Prager yield cone surface, the return to the apex should be different from that to the smooth portion of the cone. The updated hydrostatic stress must lie at the apex of the updated cone. The point
745 at the apex must satisfy

$$p_h = c \cot \phi \quad (\text{A.14})$$

where p_h is the hydrostatic stress. The above equation can also be written with the first invariant I_1 as

$$I_1 = 3c \cot \phi \quad (\text{A.15})$$

Therefore, the consistency condition can be given with the updated I_1 and hardening curve as follows

$$I_{k+1}^{trial} - 9d\gamma K_D \bar{\eta} - 9\alpha_s K_D dT = 3c(\varepsilon_{v,k}^p + 3\bar{\eta}d\gamma, dT) \cot \phi \quad (\text{A.16})$$

750 Multiplying the both sides of the equation by η gives

$$\eta(I_{1,k+1}^{trial} - 9d\gamma K_D \eta - 9\alpha_s K_D dT) - \zeta(\varepsilon_{v,k}^p + 3\eta d\gamma, dT) = 0 \quad (\text{A.17})$$

Similarly, the above equation (A.17) can be iteratively solved and the plastic multiplier $d\gamma$ can be obtained. Finally, the stress can be updated as follows

$$\sigma'_{k+1} = \left(\frac{1}{3}I_{1,k+1}^{trial} - 3d\gamma K_D \eta - 3\alpha_s K_D dT\right) \mathbf{I} \quad (\text{A.18})$$

Appendix B. Sub-matrixes of discretized equations for pressure and temperature fields

755 The corresponding sub-matrixes of discretized equations for pressure field (Eq. 57) are listed as follows.

$$\mathbf{H}_m = \frac{1}{\Delta t} \left(\frac{1}{M} + \frac{\alpha^2}{K_d} \right) \mathbf{E}_{NE} \quad (\text{B.1})$$

$$\mathbf{R}_{mf} = \frac{\delta_{mf} T_{mf}}{S_m} \mathbf{E}_{NE} \quad (\text{B.2})$$

$$\mathbf{R}_{fm} = \frac{T_{mf}}{l_{mf}} \mathbf{E}_{NE} \quad (\text{B.3})$$

where \mathbf{E} is the identity matrix.

$$\mathbf{F}_m = \left[-\alpha \frac{\varepsilon_v^{n+1,l} - \varepsilon_v^n}{\Delta t} + \frac{\alpha^2 p_m^{n+1,l}}{K_d \Delta t} + \frac{1}{M} \frac{p_m^n}{\Delta t} + 3\alpha\alpha_s \frac{T_m^{n+1,l}}{\Delta t} - (3a\alpha_s - 3\alpha_m) \frac{T_m^k}{\Delta t} - 3\alpha_m \frac{T_m^n}{\Delta t} \right] \quad (\text{B.4})$$

$$\mathbf{F}_f = \left[\frac{w_f^{n+1,l} - w_f^n}{\Delta t} \right] \quad (\text{B.5})$$

The corresponding sub-matrixes of discretized equations for temperature field (Eq. 63) are listed as follows.

$$\mathbf{D}_m = \frac{1}{\Delta t} (\rho c + 9\alpha_s^2 K_d T_0) \mathbf{E}_{NE} \quad (\text{B.6})$$

$$\mathbf{D}_f = \frac{\rho_f c_f}{\Delta t} \mathbf{E}_{N_f} \quad (\text{B.7})$$

$$\mathbf{L}_{mf} = \frac{\delta_{mf} h_t l_{mf}}{S_m} \mathbf{E}_{NE} \quad (\text{B.8})$$

$$\mathbf{L}_{fm} = \frac{h_t l_{mf}}{S_f} \mathbf{E}_{NE} \quad (\text{B.9})$$

$$\mathbf{F}_T = \left[-3\alpha_s K_d T_0 \frac{\varepsilon_v^{n+1,l} - \varepsilon_v^n}{\Delta t} + 9\alpha_s^2 K_d T_0 \frac{T_m^{n+1,l}}{\Delta t} + \rho c \frac{T_m^n}{\Delta t} + 3\alpha\alpha_s T_0 \frac{p_m^{n+1,l}}{\Delta t} - (3\alpha\alpha_s T_0 - 3a_m T_0) \frac{p_m^{k+1}}{\Delta t} - 3a_m T_0 \frac{p_m^n}{\Delta t} \right] \quad (\text{B.10})$$

760

References

Abousleiman, Y., Cheng, H.D., Detournay, E., Cui, L., Roegiers, J.C., 1996. Mandel's problem revisited. *Gotechnique* 46, 187–195.

AbuAisha, M., Loret, B., Eaton, D., 2016. Enhanced geothermal systems (egs): Hydraulic fracturing in a thermo-poroelastic framework. *Journal of Petroleum Science and Engineering* 146, 1179–1191.

765

- Aranson, I.S., Kalatsky, V.A., Vinokur, V.M., 2000. Continuum field description of crack propagation. *Physical Review Letters* 85, 118–121.
- Arogundade, O., Zhiyenkulov, M., Ajose-Ogunlana, D., 2016. Geomechanical prediction of thermal induced fractures in a reservoir, in: 50th U.S. Rock Mechanics/Geomechanics Symposium, American Rock
770 Mechanics Association. pp. 1–8.
- Barends, F., 2010. Complete solution for transient heat transport in porous media, following lauwierier, in: SPE Hydraulic Fracturing Technology Conference, Society of Petroleum Engineers. pp. 1–12.
- Bohlooli, B., Pater, C.J.D., 2006. Experimental study on hydraulic fracturing of soft rocks: Influence of fluid rheology and confining stress. *Journal of Petroleum Science & Engineering* 53, 1–12.
- 775 Brun, M.K., Wick, T., Berre, I., Nordbotten, J.M., Radu, F.A., 2020. An iterative staggered scheme for phase field brittle fracture propagation with stabilizing parameters. *Computer Methods in Applied Mechanics and Engineering* 361, 112752.
- Chau-Dinh, T., Zi, G., Lee, P.S., Rabczuk, T., Song, J.H., 2012. Phantom-node method for shell models with arbitrary cracks. *Computers and Structures* 92, 242–256.
- 780 Chukwudozie, C., Bourdin, B., Yoshioka, K., 2019. A variational phase-field model for hydraulic fracturing in porous media. *Computer Methods in Applied Mechanics and Engineering* 347, 957–982.
- Crouch, S.L., Starfield, A.M., Rizzo, F.J., 1983. *Boundary Element Methods in Solid Mechanics*. George Allen & Unwin.
- Cryer, C.W., 1963. A comparison of the three-dimensional consolidation theories of biot and terzaghi.
785 *Quarterly Journal of Mechanics & Applied Mathematics* 16, 401–412.
- Dahi-Taleghani, A., Olson, J.E., 2011. Numerical modeling of multi-stranded hydraulic fracture propagation: Accounting for the interaction between induced and natural fractures. *Spe Journal* 16, 575–581.
- Elguedj, T., Gravouil, A., Combescure, A., 2006. Appropriate extended functions for x-fem simulation of plastic fracture mechanics. *Computer Methods in Applied Mechanics and Engineering* 195, 501–515.
- 790 Elguedj, T., Gravouil, A., Combescure, A., 2007. A mixed augmented lagrangian-extended finite element method for modelling elastic-plastic fatigue crack growth with unilateral contact. *International Journal for Numerical Methods in Engineering* 71, 1569–1597.
- Erdogan, F., Sih, G., 1963. On the crack extension in plates under plane loading and transverse shear. *Journal of Basic Engineering* 85, 519–525.
- 795 Fan, W., Sun, H., Yao, J., Fan, D., Yang, Y., 2019. Homogenization approach for liquid flow within shale system considering slip effect. *Journal of Cleaner Production* 235, 146–157.
- Feng, W., Were, P., Li, M., Hou, Z., Zhou, L., 2016. Numerical study on hydraulic fracturing in tight gas formation in consideration of thermal effects and thm coupled processes. *Journal of Petroleum Science & Engineering* 146, 241–254.

- 800 Fu, P., Settghost, R.R., Hao, Y., Morris, J.P., Ryerson, F.J., 2017. The influence of hydraulic fracturing on carbon storage performance. *Journal of Geophysical Research Solid Earth* 122, 9931C9949.
- Garipov, T.T., Tomin, P., Rin, R., Voskov, D.V., Tchelepi, H.A., 2018. Unified thermo-compositional-mechanical framework for reservoir simulation. *Computational Geosciences* , 1–19.
- Geertsma, J., Klerk, F.D., 1969. A rapid method of predicting width and extent of hydraulically induced fractures. *Journal of Petroleum Technology* 21, 1571–1581.
- 805 Han, B., Shen, W.Q., Xie, S.Y., Shao, J.F., 2018. Influence of pore pressure on plastic deformation and strength of limestone under compressive stress. *Acta Geotechnica* , 1–11.
- Heider, Y., Markert, B., 2016. A phase-field modeling approach of hydraulic fracture in saturated porous media. *Mechanics Research Communications* 80, 38–46.
- 810 Huang, Z., Xia, Y., Yao, J., 2014. A two-phase flow simulation of discrete-fractured media using mimetic finite difference method. *Communications in Computational Physics* 16, 799–816.
- Ji, H., Chopp, D., Dolbow, J., 2002. A hybrid finite element/level set method for modelling phase transformation. *International Journal for Numerical Methods in Engineering* 54, 1209–1233.
- Khristianovic, S., Zheltov, A., 1955. Formation of vertical fractures by means of highly viscous liquid, in: Proc. 4th world petroleum congress, pp. 579–586.
- 815 Kim, J., Tchelepi, H.A., Juanes, R., 2011. Stability and convergence of sequential methods for coupled flow and geomechanics: Fixed-stress and fixed-strain splits. *Computer Methods in Applied Mechanics and Engineering* 200, 1591–1606.
- de Laguna, W., 1966. Disposal of radioactive wastes by hydraulic fracturing: Part i. general concept and first field experiments. *Nuclear Engineering and Design* 3, 338–352.
- 820 Lecampion, B., 2009. An extended finite element method for hydraulic fracture problems. *International Journal for Numerical Methods in Biomedical Engineering* 25, 121–133.
- Li, L., Yao, J., Li, Y., Wu, M., Zeng, Q., Lu, R., 2014. Productivity calculation and distribution of staged multi-cluster fractured horizontal wells. *Petroleum Exploration and Development* 41, 504–508.
- 825 Mandel, J., 1953. Consolidation des sols (etude mathematique). *Gotechnique* 3, 287–299.
- Mcclure, M.W., Babazadeh, M., Shiozawa, S., Huang, J., 2016. Fully coupled hydromechanical simulation of hydraulic fracturing in 3d discrete-fracture networks. *Spe Journal* 21, 1302–1320.
- Mikelic, A., Wheeler, M.F., Wick, T., 2015. A phase-field method for propagating fluid-filled fractures coupled to a surrounding porous medium. *Multiscale Modeling & Simulation* 13, 367–398.
- 830 Mohammadnejad, T., Khoei, A., 2013. An extended finite element method for hydraulic fracture propagation in deformable porous media with the cohesive crack model. *Finite Elements in Analysis and Design* 73, 77–95.
- Papanastasiou, P., 1997. The influence of plasticity in hydraulic fracturing. *International Journal of Fracture*

84, 61–79.

- 835 Papanastasiou, P., 1999. The effective fracture toughness in hydraulic fracturing. *International Journal of Fracture* 96, 127–147.
- Papanastasiou, P., Papamichos, E., Atkinson, C., 2016a. Hydraulic fracturing in co2 geological storage, in: 50th U.S. Rock Mechanics/Geomechanics Symposium, American Rock Mechanics Association. pp. 1–7.
- Papanastasiou, P., Papamichos, E., Atkinson, C., 2016b. On the risk of hydraulic fracturing in co2 geological
840 storage. *International Journal for Numerical and Analytical Methods in Geomechanics* 40, 1472–1484.
- Rabczuk, T., Zi, G., Gerstenberger, A., Wall, W.A., 2008. A new crack tip element for the phantom-node method with arbitrary cohesive cracks. *International Journal for Numerical Methods in Engineering* 75, 577–599.
- Remmers, J.J.C., Borst, R.D., Needleman, A., 2008. The simulation of dynamic crack propagation using
845 the cohesive segments method. *Journal of the Mechanics and Physics of Solids* 56, 70–92.
- Ren, G., Jiang, J., Younis, R., 2016. A fully coupled XFEM-EDFM model for multiphase flow and geomechanics in fractured tight gas reservoirs. *Procedia Computer Science* 80, 1404–1415.
- Ren, G., Jiang, J., Younis, R.M., 2018. A model for coupled geomechanics and multiphase flow in fractured porous media using embedded meshes. *Advances in Water Resources* 122, 113–130.
- 850 Réthoré, J., De Borst, R., Abellan, M.A., 2007a. A discrete model for the dynamic propagation of shear bands in a fluid-saturated medium. *International journal for numerical and analytical methods in geomechanics* 31, 347–370.
- Réthoré, J., De Borst, R., Abellan, M.A., 2007b. A two-scale approach for fluid flow in fractured porous media. *International Journal for Numerical Methods in Engineering* 71, 780–800.
- 855 Réthoré, J., De Borst, R., Abellan, M.A., 2008. A two-scale model for fluid flow in an unsaturated porous medium with cohesive cracks. *Computational Mechanics* 42, 227–238.
- Salimzadeh, S., Paluszny, A., Zimmerman, R.W., 2017. Three-dimensional poroelastic effects during hydraulic fracturing in permeable rocks. *International Journal of Solids & Structures* 108, 153–163.
- Sarris, E., Papanastasiou, P., 2013. Numerical modeling of fluid-driven fractures in cohesive poroelastoplastic
860 continuum. *International Journal for Numerical and Analytical Methods in Geomechanics* 37, 1822–1846.
- Settari, A., Walters, D.A., et al., 2001. Advances in coupled geomechanical and reservoir modeling with applications to reservoir compaction. *Spe Journal* 6, 334–342.
- Silling, S.A., 2000. Reformulation of elasticity theory for discontinuities and long-range forces. *Journal of the Mechanics & Physics of Solids* 48, 175–209.
- 865 Valko, P., Economides, M.J., 1995. *Hydraulic fracture mechanics*. Wiley Chichester.
- Wang, H., 2015. Numerical modeling of non-planar hydraulic fracture propagation in brittle and ductile rocks using xfem with cohesive zone method. *Journal of Petroleum Science and Engineering* 135, 127–140.

- Wang, X., Yao, J., Gong, L., Sun, H., Yang, Y., Zhang, L., Li, Y., Liu, W., 2019. Numerical simulations of proppant deposition and transport characteristics in hydraulic fractures and fracture networks. *Journal of Petroleum Science and Engineering* 183, 106401.
- Weng, X., Kresse, O., Cohen, C.E., Wu, R., Gu, H., et al., 2011. Modeling of hydraulic-fracture-network propagation in a naturally fractured formation. *SPE Production & Operations* 26, 368–380.
- Wilson, Z.A., Landis, C.M., 2016. Phase-field modeling of hydraulic fracture. *Journal of the Mechanics and Physics of Solids* 96, 264–290.
- Wu, K., Olson, J.E., et al., 2015. Simultaneous multifracture treatments: fully coupled fluid flow and fracture mechanics for horizontal wells. *SPE journal* 20, 337–346.
- Yalchin, E., Thomas, Y.H., 2008. *Multiscale Finite Element Methods. Theory and Applications*. Springer.
- Yan, X., Huang, Z., Yao, J., Li, Y., Fan, D., 2016. An efficient embedded discrete fracture model based on mimetic finite difference method. *Journal of Petroleum Science and Engineering* 145, 11–21.
- Yan, X., Huang, Z., Yao, J., Zhang, Z., Liu, P., Yang, L., Dongyan, F., 2019. Numerical simulation of hydro-mechanical coupling in fractured vuggy porous media using the equivalent continuum model and embedded discrete fracture model. *Advances in Water Resources* 126, 137–154.
- Yao, B., Wang, L., Patterson, T., Kneafsey, T., Yin, X., Wu, Y., et al., 2017a. Experimental study and modeling of cryogenic fracturing treatment of synthetic rock samples using liquid nitrogen under tri-axial stresses, in: *SPE Unconventional Resources Conference, Society of Petroleum Engineers*. pp. 1–10.
- Yao, B., Wang, L., Yin, X., Wu, Y.S., 2017b. Numerical modeling of cryogenic fracturing process on laboratory-scale niobrara shale samples. *Journal of Natural Gas Science and Engineering* 48, 169–177.
- Zeng, Q., Yao, J., 2016. Numerical simulation of fracture network generation in naturally fractured reservoirs. *Journal of Natural Gas Science and Engineering* 30, 430–443.
- Zeng, Q., Yao, J., Shao, J., 2019a. Effect of plastic deformation on hydraulic fracturing with extended element method. *Acta Geotechnica* 14, 2083–2101.
- Zeng, Q., Yao, J., Shao, J., 2019b. Study of hydraulic fracturing in an anisotropic poroelastic medium via a hybrid EDFM-XFEM approach. *Computers and Geotechnics* 105, 51–68.
- Zeng, Q.D., Yao, J., Shao, J., 2018. Numerical study of hydraulic fracture propagation accounting for rock anisotropy. *Journal of Petroleum Science and Engineering* 160, 422–432.
- Zhang, K., Ma, X., Li, Y., Wu, H., Cui, C., Zhang, X., Zhang, H., Yao, J., 2018. Parameter prediction of hydraulic fracture for tight reservoir based on micro-seismic and history matching. *Fractals* 26, 1840009.
- Zhang, X., Jeffrey, R.G., Thiercelin, M., 2007. Deflection and propagation of fluid-driven fractures at frictional bedding interfaces: a numerical investigation. *Journal of Structural Geology* 29, 396–410.
- Zhou, S., Zhuang, X., Rabczuk, T., 2019a. Phase field modeling of brittle compressive-shear fractures in rock-like materials: A new driving force and a hybrid formulation. *Computer Methods in Applied*

Mechanics and Engineering 355, 729–752.

Zhou, S., Zhuang, X., Rabczuk, T., 2019b. Phase-field modeling of fluid-driven dynamic cracking in porous media. *Computer Methods in Applied Mechanics and Engineering* 350, 169–198.

905 Zhu, G., Chen, h., Yao, J., Sun, S., 2019. Efficient energy stable schemes for the hydrodynamics coupled phase-field model. *Applied Mathematical Modelling* 70, 82–108.

Zhu, H., Deng, J., Jin, X., Hu, L., Bo, L., 2015. Hydraulic fracture initiation and propagation from wellbore with oriented perforation. *Rock Mechanics & Rock Engineering* 48, 585–601.